CHAPTER 4

GAS-ASSISTED EVAPORATION HEAT AND MASS TRANSFER

***Shankar Narayanan,*[1,2] *Peter A. Kottke,*[3] *Yogendra K. Joshi,*[3] *& Andrei G. Fedorov*[3,*]**

[1]Department of Mechanical Engineering, Massachusetts Institute of Technology, Cambridge, MA

[2]Currently, Department of Mechanical, Aerospace and Nuclear Engineering, Rensselaer Polytechnic Institute, Troy, NY

[3]Department of Mechanical Engineering, Georgia Institute of Technology, 337 Ferst Drive, Atlanta, GA 30332

[*]Address all correspondence to: Andrei G. Fedorov, E-mail: agf@gatech.edu

Evaporation plays a critical role in nature and many industrial applications. Evaporation has been studied extensively to address extreme thermal challenges in electronics. This chapter presents an overview of evaporation-based cooling techniques, followed by a detailed description and performance characterization of two novel techniques that leverage gas-assisted thin film evaporation. These methodologies combined can potentially address both localized and averaged cooling requirements, which are critical bottlenecks in high-performance microelectronics. One of the techniques utilizes a novel hybrid thermal management device, which improves the performance of conventional air-cooled heat sinks using on-demand and spatially controlled droplet impingement evaporative cooling. The other cooling methodology makes use of microscopically thin liquid films to provide efficient heat and mass transfer. In this technique, the use of nanoporous membranes maintains thin liquid films, minimizing the possibility of dry-out by exploiting capillary confinement of the fluid. In combination with flow of dry air, this arrangement yields record high heat and mass fluxes. A detailed computational analysis is carried out to determine the relative effects of the performance-governing parameters, which is also supported by experiments, using a microscale device supporting gas-assisted thin film evaporation. While the understanding gained in these techniques enables dissipation of high heat fluxes for electronic cooling, it is also relevant in applications relying on efficient evaporation and phase separation such as membrane distillation and climate control systems.

KEY WORDS: *evaporation, phase-change, thin film, nanoporous membrane, electronic cooling, spray cooling, high heat flux, water purification, membrane distillation, desalination*

1. INTRODUCTION

Evaporation plays a critical role in nature and myriad industrial applications. Among the emerging technologies for desalination, membrane distillation takes advantage of evaporation across a hydrophobic membrane, and promises a viable option for water purification.[1] Evaporation and condensation processes are known to affect the overall performance of fuel cells due to significant heat transfer associated with these physical mechanisms and dependence of polymer membrane ionic conductivity on hydration.[2,3] The understanding

ISSN: 1049–0787; ISBN: 978–1–56700–454–0/16/$35.00 + $00.00

NOMENCLATURE

A	Hamaker's constant, J
Br	Brinkman number
c	specific heat, J/kg K
c_{pl}	specific heat of the liquid phase, J/kg K
d_h	hydraulic diameter, m
D	membrane leading edge offset, m
D_{K}	coefficient of combined Knudsen-molecular diffusion, m^2/s
e	elementary charge (1.60217662 × 10^{-19} C)
h	Planck's constant (6.626068 × 10^{-34} m^{2}kg/s)
h'	mass transfer coefficient, m/s
h_{fg}	latent heat of vaporization, J/kg K
h'_{ref}	mass transfer coefficient at reference conditions, m/s
h_{T}	heat transfer coefficient, W/m^2 K
$h_{\mathrm{T,ref}}$	heat transfer coefficient at reference conditions, W/m^2 K
H	microchannel height, m
k	thermal conductivity, W/m K
k_{al}	thermal conductivity of porous anodic alumina membrane, W/m K
k_{B}	Boltzmann constant (1.3806503 × 10^{23} m^{2}kg/s^2 K)
k_{l}	thermal conductivity of the liquid phase, W/m K
k_{p}	thermal conductivity of Pyrex substrate, W/m K
k_{v}	thermal conductivity of the vapor phase, W/m K
$\dot{m}$	mass flow rate, kg/s
$\dot{m}''$	mass flux, kg/m^2 s
M	molecular weight, kg/mol
n	correlation number used to obtain h_{T} with $h_{\mathrm{T,ref}}$
n_i	refractive index of the medium (where $i = 1$, 2, and 3)
p_{atm}	atmospheric pressure, Pa
p_{l}	pressure of liquid phase, Pa
p_{li}	pressure of the liquid phase at the liquid-vapor interface, Pa
p_{v}	vapor pressure away from the interface, Pa
$p_{\mathrm{v,eq}}$	equilibrium vapor pressure, Pa
p_{vi}	vapor pressure at the interface, Pa
P_{ref}	reference pressure (atmospheric pressure), Pa
$\dot{q}'''_j$	volumetric heat generation rate, W/m^3
$\dot{q}'''_{\mathrm{m}}$	average volumetric heat sink for the membrane region, W/m^3
r	radial coordinate, m
r_{c}	radius of the nanopore, m
r_{i}	radial position of the interface, m
R	universal gas constant, J/mol K
Re_{j}	Reynolds number corresponding to the air jet
Re_{l}	Reynolds number for the liquid phase flow
T	temperature, K
T_{air}	temperature of ambient air, K
T_{l}	temperature of the liquid phase, K
T_{li}	temperature of the liquid phase at the interface, K
T_{p}	temperature of the Pyrex substrate, K
T_{s}	temperature of the silicon substrate, K
T_{v}	temperature of the vapor phase away from the interface, K
T_{vi}	temperature of the vapor phase at the interface, K
T_{vo}	temperature of the vapor phase at the membrane outlet, K
$T_{\mathrm{v}\infty}$	temperature of the vapor phase in the far field, K
T_{w}	temperature of the nanopore wall, K
$\bar{u}_{\mathrm{l}}$	velocity of the liquid phase, m/s

NOMENCLATURE (*continued*)

u_{l}	axial component of the velocity of the liquid phase, m/s
u_{li}	axial component of the velocity of the liquid phase at the interface, m/s
v_{l}	radial component of the velocity of the liquid phase, m/s
v_{li}	radial component of the velocity of the liquid phase at the interface, m/s
w_{li}	normal component of velocity of the liquid phase at the interface, m/s
W_{H}	hotspot width, m
W_{M}	membrane width, m
x	axial coordinate, m
$X_{\mathrm{v,eq}}$	equilibrium mole fraction of the vapor phase
X_{vi}	mole fraction of the vapor phase at the interface
X_{vo}	mole fraction of the vapor phase at the membrane outlet
$X_{\mathrm{v}\infty}$	mole fraction of the vapor phase in the far field
Z	charge number of a dissociated ion

Greek Symbols

δ_{m}	thickness of the nanoporous membrane, m
δ_{v}	location of the meniscus relative to the membrane outlet, m
ε	membrane porosity
ε_{i}	dielectric constant (i $= r$, 1, 2, and 3)
ε_{o}	permittivity of free space, F/m
κ	curvature of meniscus, 1/m
μ_{l}	dynamic viscosity of the liquid phase, kg/ms
ν_e	absorption frequency, 1/s
ν_{l}	kinematic viscosity of the liquid phase, m^2/s
Π_{d}	disjoining pressure, Pa
ρ_{l}	density of liquid phase, kg/m^3
ρ	density, kg/m^3
ρ_{sat}	vapor density in saturation conditions, kg/m^3
σ	surface tension, N/m
$\hat{\sigma}$	accommodation coefficient
θ	slope of the interface at any particular location

of evaporation is also crucial for fire extinguishing operations, wherein the droplet size of water sprays can control the efficacy of fire retardation.[4] Evaporation of fuel droplets is important for elucidating combustion and extraction of maximum energy from fossil fuels.[5−7] For indoor swimming pools, the rate of water evaporation is of considerable interest, since it can consume the highest energy in heating, ventilation, and air-conditioning (HVAC) systems.[8,9] On relatively smaller length scales, evaporation of thin liquid films laden with colloidal particles can result in self-assembly, which in turn yields crystalline macroporous materials for manufacturing photonic bang gap materials, waveguides, antireflective coatings, sensors, magnetic storage media, and novel lithographic applications.[10−13] As evaporation has emerged to be of critical importance, one of its crucial applications has been in electronic cooling, as described below.

The process developments in the semiconductor industry have led to the use of higher power, enhanced functionality, and reduced feature sizes in electronics, which has resulted in significant average and localized heat generation.[14] Therefore, efficient thermal management is critical to ensure reliable performance of electronic devices. Traditionally, air-cooled heat sinks have been used for electronics. However, with a maximum heat transfer coefficient of only $\sim 10^3$ W/m^2 K,[15] there is a fundamental limit on achievable cooling performance while maintaining low operational temperatures. On the other hand, single-phase liquid cooling can provide much higher performances of $\sim 10^4$ W/m^2 K, if relatively high pumping power can be tolerated for flow in microchannel heat sinks.[16,17] Even greater improvement in cooling performance is possible without prohibitively high liquid pumping power by leveraging the latent heat of phase change, via either boiling or evaporation. Pool boiling has been extensively studied with a wide range of liquids, surface-enhancing features, and operational conditions to demonstrate significant cooling with local heat transfer coefficient exceeding $\sim 10^4$ W/m^2 K.[18] Further improvement can be achieved by convective boiling in microchannels, with heat transfer coefficient exceeding 10^4 W/m^2 K.[19] Although phase change via boiling has clearly enhanced the maximum achievable heat fluxes, numerous factors including boiling incipience, bubble nucleation and departure, control of dry-out, and critical heat fluxes (CHFs) pose challenges for further enhancements in cooling performance.

The emerging demands of electronics, which feature a combination of substantial background (average ~ 100 W/cm^2) heat fluxes over larger areas, and even higher "hotspot" heat fluxes (~ 1000 W/cm^2) over smaller domains, require new approaches and novel devices with significant enhancement in cooling performance. Contrary to boiling or phase change in the bulk liquid, evaporation can occur at the free surface of a liquid at relatively lower temperatures, when the interface is exposed to subsaturation and dry conditions. In this chapter, we discuss the fundamental challenges and opportunities in leveraging evaporation to yield effective cooling with heat transfer coefficients that can potentially exceed 10^4 W/m^2 K with minimal power for coolant circulation. Along with a brief overview of the techniques leveraging evaporative cooling for heat dissipation, this chapter presents two new techniques in detail that leverage gas-assisted evaporation, to address the rise in background and localized heat fluxes found in high-power electronics.

Section 2 provides a brief overview of various techniques that leverage evaporative cooling for heat dissipation. In Section 3, we discuss the operation and performance of a hybrid thermal management device, which enables enhancement in conventional air-cooled heat sinks using on-demand and spatially controlled droplet/jet impingement evaporative cooling. This section describes the design and operation of the device, and highlights experimental characterization of the device performance. Section 4 describes a unique technique for enabling gas-assisted evaporation of thin liquid films using nanoporous membranes. Since the cooling technique utilizes a nanoporous membrane, the interfacial transport in nanopores is first characterized using a semi-analytical modeling approach (Section 4.1). Subsequently, a microscale device enabling thin film evaporation is described. A detailed study of the device performance, via both computational and experimental analysis, is described in Section 4.2. Section 5 summarizes the chapter with a brief discussion of future directions in enabling efficient evaporation through nanoporous membranes.

2. HEAT DISSIPATION USING EVAPORATIVE COOLING

Heat dissipation via evaporation of thin liquid films has been demonstrated in various electronic cooling strategies. In the last decade, these strategies haven taken advantage of evaporation of water, as well as dielectric liquids via the use of shear-driven liquid flow,[20] spray or mist cooling,[21−26] micro- and nanostructures,[27−29] and chemically functionalized surfaces.[30,31] Evaporation from spray impingement delivers performance exceeding 10^4 W/m^2 K,[24] which is further enhanced by incorporating microstructures.[22,23] More interestingly, cooling strategies incorporating nanostructures and hierarchical features have been able to deliver heat dissipation in excess of 10^5 W/m^2 K.[28] To maximize heat dissipation from surfaces, these strategies have a common underlying objective: the use of very thin liquid films to minimize thermal resistance. Various cooling techniques pursue this crucial underlying objective in different ways, as elaborated in the following section.

2.1 Evaporative Cooling using Spray Impingement

Evaporation using spray and mist cooling systems has been applied to thermal management of electronic devices. Heat transfer characteristics of spray cooling using water on plain and microstructured silicon surfaces have been studied in detail,[23] wherein it was found that the capillary forces within the microstructures are effective in spreading the liquid film, thus promoting evaporation rates. In another study, MEMS-based evaporative, spray cooling devices have been tested for thermal management of high heat flux electronics using dielectric coolants.[32] In addition to using microstructures on the impinging surfaces, this study elucidates the effect of different micronozzle orifice geometries. The microstructures were found to deliver better cooling performance than plain surfaces, and support higher fluxes before the liquid film breaks up since more water was retained due to the capillary forces. However, microstructures were found to provide no noticeable enhancement when the surface was completely flooded. Heat transfer coefficients of 10^3–10^4 W/m^2 K were achieved using spray cooling on textured surfaces.[21,23,24,33] Higher operational temperatures resulted in the loss of thin films and led to the formation of dry spots, which was detrimental to sustaining cooling. The heat transfer coefficients and temperature stability deteriorated greatly once the liquid film breakup occurred.

In addition to conventional spray cooling, electrospray evaporative cooling has also been investigated for thermal management of electronics.[5,34] This methodology relies on coulombic forces for energy-efficient fluid atomization. Conventional spray cooling results from the impact of droplets on a heated surface, which may lead to rebound. As a result, in conventional sprays, only a fraction of the liquid cooling capacity is exploited due to the rebound effect. Electrospray was found more promising since droplet rebound from the surface was prevented completely. In electrospray, once the droplets are charged, it is observed that if the droplet impact time is less than the charge relaxation time, the charge leakage from the droplet to the impinging substrate is relatively slow. As the droplet is still charged after impact, it experiences an additional coulombic attraction force, or image force, with the substrate. For picoliter droplets, the image force is three orders of magnitude larger than gravity and can help prevent rebound, which was confirmed with high-speed imaging.[34]

2.2 Evaporative Cooling using Micro- and Nanoporous Structures

Porous media have also found extensive use in thermal management of electronics. Specifically, phase change in micro- and nanoporous materials is found promising for the dissipation of high heat fluxes with near-isothermal conditions, since it offers several advantages, including high surface area-to-volume ratio, favorable wetting characteristics, and high thermal conductivity. Copper has been one of the most attractive materials for heat transfer applications due to its high thermal conductivity and inexpensive processing. However, poor wettability of water on copper surfaces can compromise the overall phase change and heat transfer performance.[35,36] Controlled chemical oxidation of copper has been carried out to render superhydrophilicity to the wetting surface by the growth of copper oxide nanostructures. Wetting surfaces consisting of copper oxide nanostructures on microscale copper posts were shown to result in enhanced phase change, and heat transfer coefficients exceeding 10^5 W/m^2 K.[28] Similarly, multiscale structures using carbon nanotubes on microporous sintered copper provide enhanced thermal transport and permeability to support high heat fluxes.[37] More recently, a cooling device capable of dissipating large heat fluxes using evaporation was proposed,[29] wherein perforated microchannels were used to separate liquid and vapor flows. The phase-separating microchannel device was designed to take advantage of extended surfaces in the perforated channels for evaporation, while separating vapor and liquid flows to eliminate flow instabilities associated with flow boiling. While experimental results are not yet available, theoretical predictions show dissipation of high heat fluxes ($>10^3$ W/cm^2), using dielectric fluids with manageable ($\sim 10^3$ Pa) pressure drops. The use of microstructures to maintain thin liquid films and enhance cooling has also been explored to demonstrate dissipation of high heat fluxes ($>10^2$ W/cm^2) using both boiling and evaporation as the mode of heat transfer for thin capillary wicking structures.[38,39]

2.3 Evaporative Cooling using Electrowetting

Unlike using spray, micro- and nanostructured surfaces for evaporative cooling, electrowetting offers another technique to maintain thin evaporating liquid films for thermal management. Electrowetting on dielectric (EWOD)[31] is expected to have great potential because EWOD-driven droplet transport has a prompt response, low power consumption, and programmable paths without the need for any mechanical moving parts. Consequently, electrowetting transport techniques have been developed for chip cooling. Furthermore, EWOD-assisted dropwise evaporation/boiling has been demonstrated for adaptive cooling of microelectronics.[40,41] Using porous wetting surfaces on heated regions, thin evaporating films could be sustained with precisely controlled volumes of droplets delivered continuously using the electrowetting phenomenon. With the EWOD-based fluidic operations, such as droplet splitting and merging, the droplet volume can be accurately confined for real-time thermal management applications.[31,41]

2.4 Gas-Assisted Evaporative Cooling

The concept of gas-assisted evaporative cooling of electronics was first demonstrated with the injection of a gas stream to disperse a liquid coolant flowing within a channel, thereby promoting evaporation and increasing heat transfer.[42,43] In a related technique, water spray, and high-speed airflow, have been demonstrated for dissipating heat in electromagnetic rail guns by combining spray and evaporative cooling.[24] By varying the liquid supply nozzle pressures and airflow velocities, heat transfer coefficients exceeding 2 × 10^4 W/m^2K have been demonstrated.[24]

In addition to evaporation via spray cooling and the use of micro- and nanostructures, the use of shear-driven liquid films, primarily led by Kabov et al.,[20,45–55] has also been pursued for cooling applications. Typically, this technique utilizes two-phase flow, where a gas or vapor is forced along a channel, and due to shear stress at the liquid-gas/vapor interface, a liquid film is also set in motion. This method is expected to result in high heat fluxes since heat is transferred to a thin evaporating liquid film moving in a microchannel under friction of a forced gas or vapor flow. In order to leverage this technique, several experimental[20,44–49] and numerical studies[50–55] have been carried out. These investigations elucidate the role of the evaporating fluid,[20,44,46] thermocapillary stress,[44,45,48,50,55] gravity,[46,50–52,55] wall slip,[46] gas and liquid flow configurations,[20,45,47,49,50,55] location and size of heating elements,[52] multimode heat transfer,[53] and temperature dependence of fluid properties.[54] These efforts have led to a better understanding of flow hydrodynamics and heat transfer of shear-driven flows, and demonstration of cooling performances exceeding 250 W/cm^2.[47] Although heat fluxes $>10^2$ W/cm^2 have been demonstrated, these studies highlight the challenges of sustaining a shear-driven flow and avoiding film rupture and complete dry-out.

Apart from the techniques listed above, evaporation of thin liquid films has been a topic of exhaustive research. While the following sections describe in detail two techniques enabling gas-assisted thin-film evaporation, a general overview of thin-film evaporation can be found in Ref. 56.

3. EVAPORATION-ENHANCED, DYNAMICALLY ADAPTIVE, AIR-COOLED HEAT SINK

This section summarizes the main results of our study on evaporation-enhanced air cooling, closely following the discussion in the Ref. 57. A hybrid approach is employed by integrating the mist delivery into airflow of a conventional heat sink, as shown in Fig. 1. The off-the-shelf heat sink (Fig. 2) is modified by adding a planar MEMS ultrasonic droplet ejector array as a capping surface of the finned structure. The ejected droplets with sufficient ejection velocity are readily entrained by the gas flow, resulting in orientation-independent operation. The droplets are carried by primary airflow supplied by a fan to facilitate partial liquid evaporation (and subcooling) of the carrier gas, as well as high-velocity impingement of remaining mist onto the finned surface. The latter not only enhances convective heat transfer to the evaporating liquid, but also induces uniform spreading of the evaporating liquid film over the extended surface of the heat sink. The extended surface (fins) can be engineered to be highly wetting via surface micro-/nanostructures,[58] to facilitate an effective droplet spreading and formation of thin liquid film to promote evaporation. Finally, capping of the heat sink with the planar structure of the ejector array (Fig. 1) establishes a closed gas flow conduit to prevent any parasitic air bypass of the heat sink finned area.[59] Collectively, these design innovations result in significant enhancement of the heat sink capabilities for heat dissipation over large areas, much greater than what could be achieved by using only air-based cooling.

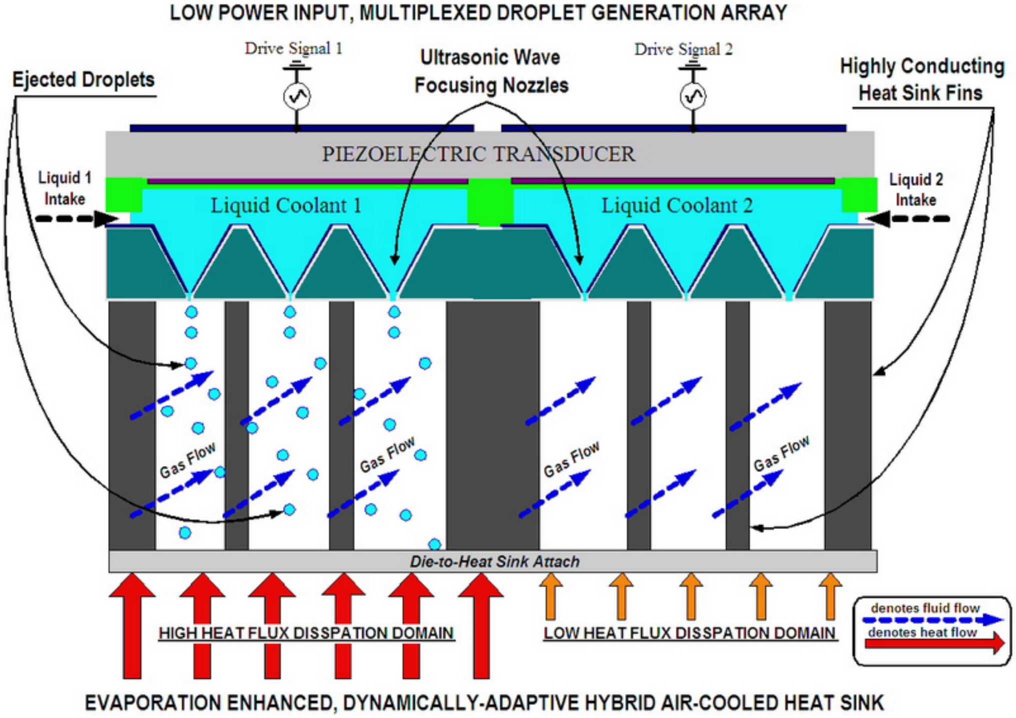

FIG. 1: Schematic of the concept for liquid evaporation-enhanced hybrid heat sink (reprinted with permission from IEEE, Copyright 2009).[57]

The device utilizes the ultrasonic droplet generator array, which is capable of on-demand delivery of mist in either the drop-on-demand mode or the continuous-jet-ejection mode.[60−62] The ejector operation modes can be selected and tuned to match the needs of specific tasks, such as droplet-to-heat sink contact time, coolant consumption control and airflow rate, and dynamically varying heat load. The ultrasonic atomizer exploits resonant operation to enable low-power mist generation, including a self-pumping capability enabled by the flexing piezoelectric transducer, which is an important consideration for power efficiency of the cooling scheme.

Figure 2(a) shows the experimental setup used for performance characterization of the hybrid heat sink. It consists of a fan with a ducted conduit that directs airflow across a standard aluminum heat sink. A polyimide flexible heater was used to emulate the power dissipation of an electronic device and several thermocouples were attached into the spreader, as shown in Fig. 2(c). The heater-heat sink assembly was thermally insulated from the environment, and the converging tunnel was used to direct the fan airflow over the extended area of the heat sink. To exemplify the cooling performance enhancement, experiments have been conducted for evaluating the degree of subcooling of the heat spreader when mist impingement evaporation is initiated, as compared to purely air cooling [Fig. 2(b)]. Further details on the experimental procedure can be found in Ref. 57.

The results indicate that for different fan flow rates, the maximum spreader temperature can be reduced by $\sim$15% with the introduction of mist impingement, which translates to

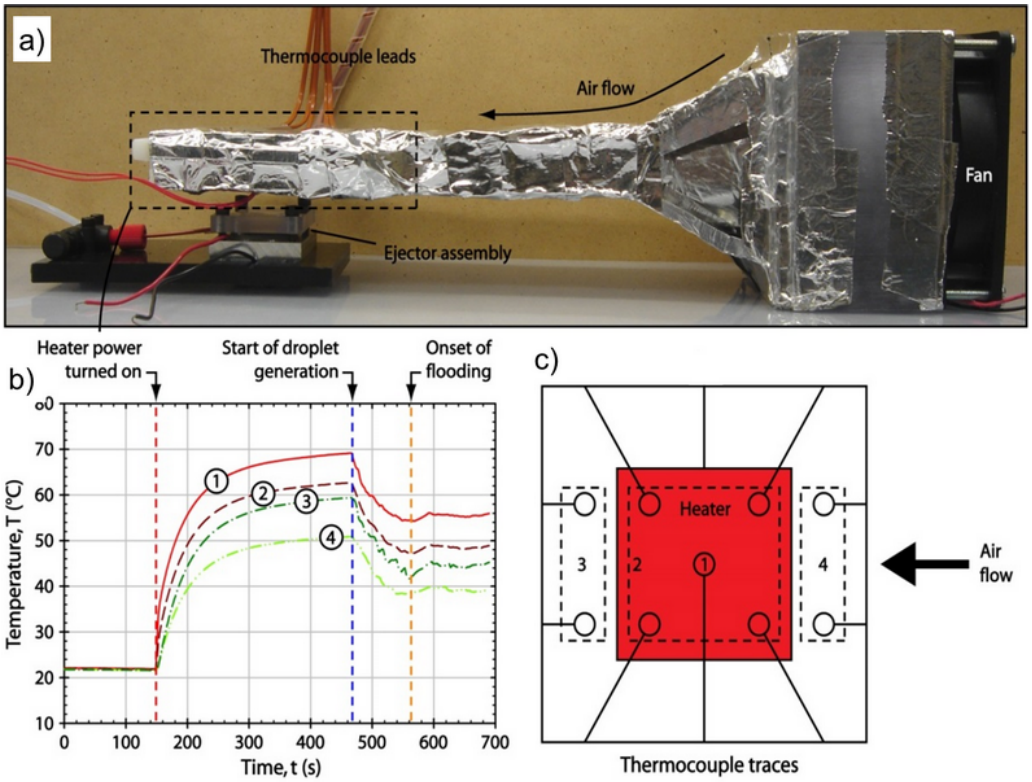

FIG. 2: (a) Experimental setup for evaluation of performance enhancement via evaporative cooling. (b) Fan with ducted outlet directing airflow through the fins of an aluminum heat sink outfitted with ultrasonic ejector array for mist delivery. (c) Lines 1, 2, 3, and 4 represent the maximum heat sink temperature, the average temperature of the five heater thermocouples, and the averages of the thermocouples highlighted and labeled “3” and “4” as denoted in a diagram of the heater location and thermocouple traces (reprinted with permission from IEEE, Copyright 2009).[57]

∼25–30% increase in an effective heat transfer coefficient. Figure 2(b) shows the transient response of the air-cooled system, as the heater power is instantaneously increased from 0 to 31.3 W until a steady state is reached. At $t = 470$ s, mist impingement cooling is initiated, which results in the decrease in system temperature from 69°C to 54°C. This represents a 50% improvement in system performance. The heat sink temperature decreases until flooding of the heat sink results in a loss of performance enhancement, which was visible via inspection during the experiments.

In many evaporative cooling strategies pursued thus far, as the heat flux is increased, the liquid film was found to break easily, leading to a dry spot and a local decrease in the heat transfer coefficient. This causes an increase in the surface temperature and eventually the failure of the cooling mechanism. Thus, the main challenge associated with developing an efficient and reliable evaporative cooling scheme has been to maintain a very thin ($\sim 10^{-6}$ m) and stable liquid film. Although considerable success with evaporative cooling has been reported, sustained evaporation with potentially higher heat fluxes was considerably difficult. To address the challenge of maintaining a stable liquid film with controllable thickness while maximizing the evaporation rate, membrane-enabled gas-assisted thin film evaporation can be carried out, as described below.

4. GAS-ASSISTED EVAPORATION USING NANOPOROUS MEMBRANES

The rate of evaporation and transport at the free surface of a liquid film is controlled by two fundamental resistances, i.e., the thermal conduction resistance across the liquid film, and the vapor transport resistance from the evaporating interface to the ambient environment. The film conduction resistance is controlled by the thickness and thermal conductivity of the liquid film. The vapor transport resistance is controlled by three key parameters, which are associated with the gas surrounding the liquid film and the choice of the evaporating liquid. These parameters are the mass transfer coefficient, the relative humidity of the surrounding gas, and the vapor density of the evaporating liquid. Since thermal conduction and vapor transport resistances act in series, it is important to minimize both to achieve the highest rate of heat transfer via evaporation, which can be accomplished as follows.

In membrane-enabled gas-assisted evaporation, a liquid is pumped into a micro-cavity of desired dimensions, so that the film thickness is imposed by the structure of the cavity (Fig. 3), rather than by flow conditions or hydrodynamics that are not easily controllable. The use of a micro-cavity also allows precise control of the liquid film. Consequently, it can be as thin as possible ($\sim 10^{-6}$ m) to minimize the thermal conduction resistance. This technique can also avoid dry-out, since sufficient pressure head can be maintained to keep the micro-cavity filled with liquid. To enable evaporation from the free surface of the cavity, the capping surface is constructed using a highly porous membrane with a dense array of holes to provide a pathway for the evaporating vapor, which is eventually

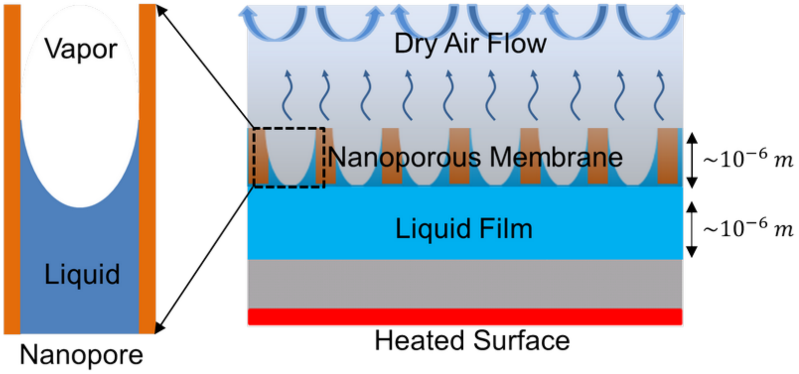

FIG. 3: The schematic illustrates the underlying concept of gas-assisted evaporative cooling, wherein a nanoporous membrane is used to confine liquid over a heated surface by capillary action. Consequently, a very thin liquid film (~ 1 μm) can be maintained. The pores in the membrane provide a pathway for vapor diffusion and eventually advection by dry air.

entrained by the surrounding gas (Fig. 3). The overall mass transfer of the vapor phase is maximized by utilizing a dry sweeping gas. The use of a highly porous membrane with small pores (10^{-8}–10^{-7} m) imposes a significant capillary force on the liquid. This can support a large pressure difference between the liquid inside the cavity and the ambient gas, allowing confinement of the liquid within the cavity. Since the capillary forces are inversely proportional to the pore radii, nanoporous membranes can support a high pressure differential. Moreover, the capillary forces can also be controlled or enhanced via selective chemical functionalization of the membrane surface in contact with the evaporating liquid.

The following sections provide a detailed description of the underlying physics controlling fluid flow and heat transfer, to gain a better understanding of thin film evaporation enabled by the use of nanoporous membranes. These sections summarize the main results of our study on gas-assisted thin film evaporation using nanporous membranes, closely following the discussion in Refs. 63–67. First, it is necessary to establish the role of nanoporous membranes, which confine the liquid in the cavity via capillary action. Since the membrane can increase the overall impedance to the vapor transport, which includes both vapor diffusion and interfacial resistance, a detailed understanding of wetting characteristics is necessary to determine interfacial transport in nanopores. The following mathematical model describes the phase change and transport during evaporation inside a cylindrical nanopore.

4.1 Interfacial Transport of Water Confined in Nanopores

In order to analyze wetting and interphase transport, it is essential to identify all the relevant factors affecting contact line dynamics. Capillarity alone has been extensively studied for interpreting the wetting phenomenon, and its relation to the chemical constitution of both solid and liquid was used to explain the extent of spreading and the equilibrium contact angle during partial wetting.[68] However, as the length scale decreases further (below 1 μm), long-range interactions such as van der Waals forces play an important role in addition to surface tension. This affects the interface shape as well as the rate of interfacial heat and mass transfer due to phase change. The forces due to dipole induction and molecular orientation and dispersion, which contribute toward the long-range interaction between molecules, are collectively known as the van der Walls forces. Among different forces, dispersion is always present between molecules and is generally dominant, as compared to the dipole-dependent induction and orientation forces, which are also known as the Debye and Keesom interactions, respectively.[69] The dispersion interactions between surfaces decay rapidly at longer separations due to attenuation of electromagnetic coupling. For very short and long distances, disjoining pressure is often given by $\Pi_\mathrm{d} = -A_0/6\pi\delta^3$ and $\Pi_\mathrm{d} = -B/\delta^4$, respectively, where A_0 is the non-retarded Hamaker's constant and B is the retarded dispersion constant.[70] Although dispersion interactions are significant in determining the disjoining pressure in the case of nonpolar liquids, electrostatic interaction between molecules should also be considered for polar solvents.

The presence of both dispersion and electrostatic interaction between two interacting media is addressed by the Derjaguin-Landau-Verwey-Overbeek (DLVO) theory.[71,72] Although DLVO theory can quantitatively describe electrostatic contribution toward surface forces in thin liquid films, it is now understood that "non-DLVO" interactions can also exist. From experimental observations, prior studies have estimated the effect of "structural interactions" in thin liquid films due to the forces other than van der Waals and DLVO interactions.[73–76] The structural component of disjoining pressure arises when interphase boundary layers, whose structure is different from that of the bulk liquid, overlap. Supported by experimental measurements, the structural component of disjoining pressure was found to decay exponentially with distance.[75] However, with dissolved ions in water, these forces still fail to explain the behavior of many colloidal systems. The concept of short-range hydration forces was then introduced to relate theory to experiments based on interaction of a mica surface with electrolyte solutions.[77] But this concept has also been met with some skepticism,[78] and is still amid validation. More recently, there are concepts based on additional interaction modes, which include image charge forces, steric interactions, and hydrophobic forces that try to explain the experimental observations. Given the uncertainty in establishing and estimating the universally applicable force interactions, a comprehensive investigation of interfacial transport in water films is challenging and currently incomplete.

In the following section, a simplified analysis is carried out to identify the prominence of different interactions for sustaining flow, mass, and energy transport in an evaporating liquid film confined within a nanoscale capillary. Evaporation of simple, nonpolar wetting liquids has been reported to elucidate effects arising due to van der Waals interactions, in addition to capillarity. In this regard, it is noteworthy to acknowledge the contributions of Wayner and coworkers in both theoretical developments and experimental validation.[79–81] Additionally, experimental studies[82–87] and computational analyses[88–93] of thermocapillary convection and velocity slip in channels during phase change[89] are of relevance to the problem being analyzed in the following section.

In the analysis of phase change of fluids in confined spaces, the rate of evaporation at the free surface requires modification from the commonly used expression given by Schrage.[94] In other words, the change in equilibrium vapor pressure over a capillary meniscus, as compared to a "flat" interface, has to be accounted for using the Kelvin equation,[95] which is modified to include the effect of an adsorbed liquid film and presence of disjoining pressure.[96–98] Using interferometry, it has been shown that the predictions from the modified Kelvin equation match well with experimental measurements for capillary radii as small as a few nanometers.[97] Interfacial transport of nonpolar liquids is now well understood for evaporation in simple geometries like microchannels and cylindrical tubes.[80–82,88,89,99,100] However, the underlying solid-liquid-vapor interactions in previous studies were limited to dispersion and capillarity, while the effect of electrostatic interactions, which are of much longer range, becomes important in the case of polar liquids confined in nanopores. The following section presents, in brief, the mathematical analysis of fluid flow and heat transfer during evaporation of water confined in nanopores. Further details of this analysis can be found in Ref. 66.

4.1.1 *Mathematical Analysis of Flow and Heat Transfer in Nanopores*

At steady state, the shape of an evaporating interface inside a channel or pore is often broadly divided into multiple regions, as shown in Fig. 4. A thin adsorbed film in

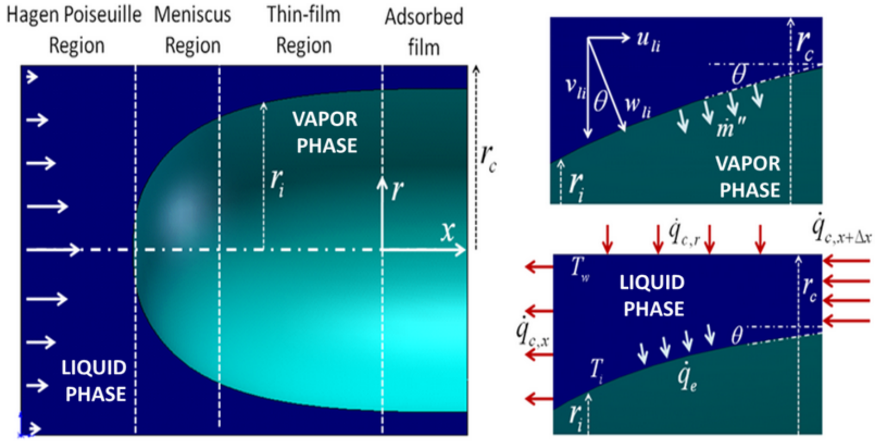

(a) (b)

FIG. 4: (a) Classification of the extended meniscus during evaporation. Note that this nanopore is oriented horizontally, as compared to the pores oriented vertically in Fig. 3. This is still consistent since the role of gravity in this analysis is insignificant. (b) Schematic for evaluation of normal interfacial velocity and illustration of various boundary heat fluxes (reprinted with permission from the American Chemical Society, Copyright 2011).[66]

equilibrium with gaseous phase forms the leading edge of the liquid-vapor interface. The adjacent region consists of a thin-film, which is influenced significantly by the disjoining pressure. The next location is denoted as the meniscus region where capillary pressure is a dominant force. Beyond the meniscus region, the flow is fully developed, laminar, and can be described by the Hagen-Poiseuille equation. In the following analysis, the origin of the cylindrical coordinate system is located at the junction of the evaporating thin film region and the adsorbed film, as shown in Fig. 4. With all the required boundary conditions defined at the origin, numerical integration is carried out with respect to the axial coordinate, x, to compute other flow variables. The position of the interface is denoted by $r_{\mathrm{i}}(x)$.

In addition to assuming a steady, axisymmetric, incompressible flow, the model described herein neglects the hydrostatic pressure and radial pressure gradient compared to the dominant capillary, disjoining pressure, and axial pressure gradients. With these assumptions, the axial component of momentum balance for liquid flow is given by

$$-\frac{dp_{\mathrm{li}}}{dx}+\frac{\mu_{\mathrm{l}}}{r}\frac{\partial}{\partial r}\left(r\frac{\partial u_{\mathrm{l}}}{\partial r}\right)=0 \tag{1}$$

The boundary conditions for fluid flow are no slip at the walls, $u=0$ at $r=r_{\mathrm{c}}$, and thermocapillary stress balance at the interface, $-\mu_{\mathrm{l}}(\partial u/\partial r)=(\partial\sigma/\partial x)$ at $r=r_{\mathrm{i}}$.[99] The solution to the differential equation (1) with these boundary conditions is therefore given by

$$u_{\mathrm{l}}=\left(-\frac{1}{4\mu_{\mathrm{l}}}\frac{dp_{\mathrm{li}}}{dx}\right)\left(r_{\mathrm{c}}^{2}-r^{2}+2r_{\mathrm{i}}^{2}\ln\frac{r}{r_{\mathrm{c}}}\right)-\frac{r_{\mathrm{i}}}{\mu_{\mathrm{l}}}\frac{\partial\sigma}{\partial x}\ln\frac{r}{r_{\mathrm{c}}} \tag{2}$$

The mass flow rate at any axial position can be obtained by integration, $\int \rho_{\mathrm{l}}u_{\mathrm{l}}(2\pi r)\,dr$ between $r=r_{\mathrm{i}}$ and $r=r_{\mathrm{c}}$, to yield

$$\begin{aligned}\dot{m} &= \frac{\pi\rho_\mathrm{l}}{8\mu_\mathrm{l}}\left(-\frac{dp_\mathrm{li}}{dx}\right)\left[\left(r_\mathrm{c}^2 - r_\mathrm{i}^2\right)\left(r_\mathrm{c}^2 - 3r_\mathrm{i}^2\right) - 4r_\mathrm{i}^4 \ln\frac{r_\mathrm{i}}{r_\mathrm{c}}\right] \\ &+ \frac{\pi\rho_\mathrm{l}}{8\mu_\mathrm{l}}\left(\frac{d\sigma}{dT}\right)\left(\frac{dT_\mathrm{li}}{dx}\right)\left[4r_\mathrm{i}\left(r_\mathrm{c}^2 - r_\mathrm{i}^2\right) + 8r_\mathrm{i}^3 \ln\frac{r_\mathrm{i}}{r_\mathrm{c}}\right]\end{aligned} \tag{3}$$

The change in mass flow rate of the liquid along the axial position due to evaporation at the interface is calculated in terms of the local mass flux. At any location on the meniscus, the mass flux is given by the evaporation kinetics[94] as

$$\dot{m}'' = \frac{2\hat{\sigma}}{2-\hat{\sigma}}\left(\frac{M}{2\pi R}\right)^{1/2}\left(\frac{p_\mathrm{vi}}{T_\mathrm{li}} - \frac{p_\mathrm{v}}{T_\mathrm{v}}\right) \tag{4}$$

where p_vi is the equilibrium vapor pressure at temperature T_li, and p_v is the vapor pressure of the gas phase at temperature T_v surrounding the interface. In order to relate mass flux to the velocity of liquid phase, the mass continuity equation, $\partial u_\mathrm{l}/\partial x + (1/r)\,\partial\,(r v_\mathrm{l})/\partial r = 0$, is integrated from $r = r_\mathrm{i}$ to $r = r_\mathrm{c}$

$$r_\mathrm{i} v_\mathrm{li} = \frac{d}{dx}\int_{r_\mathrm{i}}^{r_\mathrm{c}} r\, u_\mathrm{l}\, dr + r_\mathrm{i} u_\mathrm{li}\frac{dr_\mathrm{i}}{dx} \tag{5}$$

Equation (5) assumes that $v_\mathrm{l} = 0$ at $r = r_\mathrm{c}$. Furthermore, as the interface position r_i is a function of the axial variable, the Leibniz integral rule is used to obtain Eq. (5). This equation is transformed in terms of mass flow rate to obtain

$$v_\mathrm{li} = \frac{1}{2\pi\rho_\mathrm{l} r_\mathrm{i}}\frac{d\dot{m}}{dx} + u_\mathrm{li}\frac{dr_\mathrm{i}}{dx} \tag{6}$$

The interfacial velocity of liquid directed normal to the interface $w_\mathrm{li} = \dot{m}''/\rho_\mathrm{l}$ is evaluated in terms of the velocity components and the slope of the interface, $\theta = \tan^{-1}(dr_\mathrm{i}/dx)$, as shown in Fig. 4(b). w_li is given by

$$w_\mathrm{li} = u_\mathrm{li}\sin\theta - v_\mathrm{li}\cos\theta \tag{7}$$

Using Eqs. (6) and (7), the mass flow rate at any axial location can be related to the rate of evaporation at the interface [Eq. (4)]. To simplify the analysis, the discontinuity in temperature at the interface between the liquid and gas phase is neglected by assuming local thermal equilibrium or $T_\mathrm{v} = T_\mathrm{li}$.[99]

$$-\frac{\cos\theta}{2\pi r_\mathrm{i}}\frac{d\dot{m}}{dx} = \frac{2\hat{\sigma}}{2-\hat{\sigma}}\left(\frac{M}{2\pi R T_\mathrm{li}}\right)^{1/2}(p_\mathrm{vi} - p_\mathrm{v}) \tag{8}$$

Equation (3) relates mass flow rate to two unknown variables, namely, the pressure and temperature gradient. The pressure distribution in the liquid phase can be obtained using balance of normal stress at the interface, whereas the interfacial temperature distribution is obtained using energy conservation, as discussed below.

Although the pressure in liquid phase varies along the interface, the total pressure of the gas phase consisting of air and evaporated vapor mixture can be assumed constant and equal to atmospheric pressure p_{atm}. This assumption is based on the evaluation of Knudsen number for the transport of vapor molecules inside the cylindrical pore, which is estimated to be close to 10 for a pore radius of 25 nm. Since the corresponding flow regime is Knudsen diffusion, the pressure drop in the gaseous phase is neglected. With this assumption, the balance of normal stress across the interface is given in terms of capillary and disjoining pressures by

$$p_{\text{atm}} - p_{\text{li}} = 2\sigma\kappa + \Pi_{\text{d}} \tag{9}$$

where κ is the local mean curvature of the interface,[101] and the disjoining pressure is given by[102,103]

$$\Pi_{\text{d}} = \frac{-A}{6\pi\left(r_{\text{c}} - r_{\text{i}}\right)^3} + \frac{\varepsilon_{\text{r}}\varepsilon_{\text{o}}}{2\left(r_{\text{c}} - r_{\text{i}}\right)^2}\left(\frac{\pi k_{\text{B}} T_{\text{li}}}{Ze}\right)^2 \tag{10}$$

It is assumed that the value of surface tension remains close to the bulk value even in the thin film region. Additionally, the retardation of dispersion force is neglected in this analysis, and the van der Walls component of disjoining pressure is evaluated using the nonretarded Hamaker's constant. The Hamaker's constant for two macroscopic phases 1 and 2 interacting across a medium 3 is calculated using[69]

$$\begin{aligned} A = {} & \frac{3}{4} k_{\text{B}} T_{\text{li}} \left(\frac{\varepsilon_1 - \varepsilon_3}{\varepsilon_1 + \varepsilon_3}\right)\left(\frac{\varepsilon_2 - \varepsilon_3}{\varepsilon_2 + \varepsilon_3}\right) \\ & + \frac{3h\nu_{\text{e}}}{8\sqrt{2}} \frac{\left(n_1^2 - n_3^2\right)\left(n_2^2 - n_3^2\right)}{\sqrt{n_1^2 + n_3^2}\sqrt{n_2^2 + n_3^2}\left(\sqrt{n_1^2 + n_3^2} + \sqrt{n_2^2 + n_3^2}\right)} \end{aligned} \tag{11}$$

where ε_{i} and n_{i} (i = 1, 2, and 3) represent the dielectric constant and the refractive index of the interacting substances, respectively; k_{B} and h denote the Boltzmann's and Planck's constants, respectively; and ν_{e} denotes the absorption frequency, which is assumed to be 2.9×10^{15} s^{-1}.[104] According to Eq. (11), the Hamaker's constant varies slightly from -3.261×10^{-20} to -3.148×10^{-20} J corresponding to a temperature variation of 25 to 90°C. Therefore, in this case, a constant value of -3.148×10^{-20} J is assumed for the nonretarded Hamaker's constant.

The governing equation for interfacial temperature distribution is obtained by using the linear temperature profile and the overall energy conservation. The detailed derivation of Eq. (12) and further information on the numerical model can be found in Ref. 66.

$$\begin{aligned} & \left(2\pi k_{\text{l}} r_{\text{c}}\right)\frac{T_{\text{w}} - T_{\text{li}}}{r_{\text{c}} - r_{\text{i}}} + \frac{2\pi k_{\text{l}}}{3}\left(T_{\text{w}} - T_{\text{li}}\right)\left(\frac{dr_{\text{i}}}{dx}\right)^2 - \frac{2\pi k_{\text{l}}}{3}\left(r_{\text{c}} - r_{\text{i}}\right)\frac{dr_{\text{i}}}{dx}\frac{dT_{\text{li}}}{dx} \\ & + \frac{\pi k_{\text{l}}}{3}\left(r_{\text{c}} + 2r_{\text{i}}\right)\left(T_{\text{w}} - T_{\text{li}}\right)\frac{d^2 r_{\text{i}}}{dx^2} - \frac{\pi k_{\text{l}}}{3}\left(r_{\text{c}} + 2r_{\text{i}}\right)\left(r_{\text{c}} - r_{\text{i}}\right)\frac{d^2 T_{\text{li}}}{dx^2} = -h_{\text{fg}}\frac{d\dot{m}}{dx} \end{aligned} \tag{12}$$

Governing equations (3), (8), (9), and (12) are solved along with other auxiliary equations to determine the shape of the interface, mass flow rate, pressure, and temperature distribution. The key results obtained from this model are described below.

4.1.2 Effect of Capillary and Disjoining Pressures

The relative effects of capillary and disjoining pressures on the shape of the interface are compared in Fig. 5, corresponding to $r_{\mathrm{c}} = 30$ nm, $T_{\mathrm{w}} = 90$°C, and $p_{\mathrm{v}}/p_{\mathrm{v,eq}} = 0.98$. During evaporation, the interface acquires a distinct shape to balance the viscous stresses and pressure forces. The total interface area of the meniscus inside a capillary tube is smallest when only capillary pressure is considered, while it is largest when capillary and disjoining pressures are both included in the analysis. Away from the pore wall, where capillary forces are significantly larger than disjoining pressure, the meniscus is highly curved, resulting in higher gradient in capillary pressure to balance the viscous pressure drop inside the liquid. On the other hand, the interface is less curved and the change in slope is more gradual when disjoining pressure is significant in addition to capillary pressure near the pore wall. The presence of electrostatic interaction in addition to van der Waals forces enhances the disjoining pressure, causing a further reduction in the gradient in the curvature required to balance the viscous stress. In this analysis, it was also found that while the absolute pressure of the liquid phase is mainly determined by the capillary pressure, the disjoining pressure demonstrates a much larger gradient in the thin film region. Since gradient in pressure drives fluid flow, the contribution of electrostatic interaction is quite significant.

4.1.3 Thermocapillary Stresses in Cylindrical Nanopores

In order to determine the effect of Marangoni stress on interfacial transport, the shape of the interface is calculated for two distinct operating conditions. At $T_{\mathrm{w}} = 90$°C and $p_{\mathrm{v}}/p_{\mathrm{v,eq}} = 0.98$, the interfaces corresponding to capillary radii of 50 and 500 nm are shown in Fig. 6. For both radii, the ratio of viscous to thermocapillary stress is large, which indicates that Marangoni stresses are not significant in nano-capillaries. The shape outlined by open

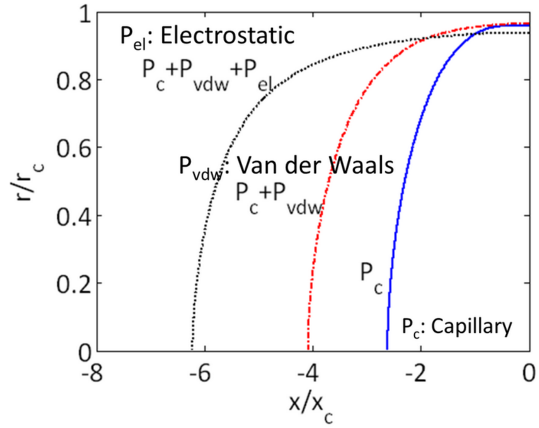

FIG. 5: The effect of capillary pressure (P_{c}), capillary and disjoining pressure ($P_{\mathrm{c}} + P_{\mathrm{vdw}}$) on the shape of the interface is illustrated. The extension of meniscus due to additional electrostatic interaction ($P_{\mathrm{c}} + P_{\mathrm{vdw}} + P_{\mathrm{el}}$) is also shown. The interface is shown for $r_{\mathrm{c}} = 30$ nm, $T_{\mathrm{w}} = 90$°C and $p_{\mathrm{v}}/p_{\mathrm{v,eq}} = 0.98$ (reprinted with permission from the American Chemical Society, Copyright 2011).[66]

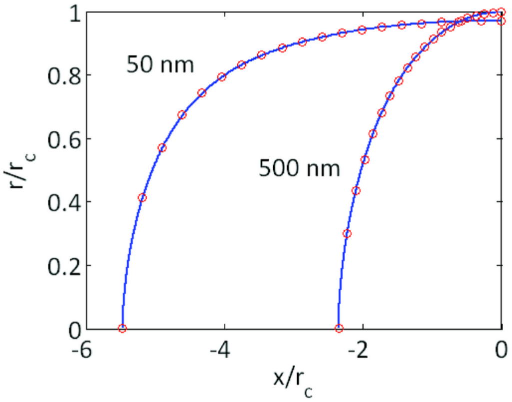

FIG. 6: The effect of thermocapillary (Marangoni) stresses for water confined in nanocapillaries. The shape of interface in capillaries of different radii, as predicted with (solid lines) and without (circles) Marangoni stresses included in the analysis. The interfaces are shown for $T_{\mathrm{w}} = 90$°C and $p_{\mathrm{v}}/p_{\mathrm{v,eq}} = 0.98$ (reprinted with permission from the American Chemical Society, Copyright 2011).[66]

circles is for viscous-shear-only transport, and is qualitatively compared with the solid curves when Marangoni stresses are included. It is clear that the inclusion of thermocapillary stresses in the analysis results in a negligible change in the interface shape for both 50 and 500 nm pores. This is expected since Marangoni stresses are prominent only in much larger capillaries with large temperature gradient along the interface. In this study, with water as the evaporating liquid, the temperature gradient is not substantial enough to affect the flow behavior even in 500 nm capillaries.

4.1.4 Effect of Wall Temperature and Vapor Pressure

Figure 7 compares the shape of the interface corresponding to different wall temperatures. The total length of the interface is smaller at higher temperatures, but yields larger average evaporation rate in a pore, as shown in the inset in Fig. 7. Since the temperature jump across the interface between the liquid and gas phase is neglected in this analysis, a higher evaporation rate for a fixed pore radius is mainly due to increase in the equilibrium vapor pressure for higher temperatures. As a result, in order to support a higher flow rate in the thin film region, a larger gradient in the interfacial curvature is expected. Consequently, the total length of the interface is also much smaller for evaporation at higher temperatures. Figure 8 compares the shape of interface resulting from varying the vapor pressure of the ambient atmosphere surrounding the evaporating meniscus for a fixed wall temperature and capillary radius. The average mass flux per pore area (πr_c^2) is directly proportional to the pressure differential at the interface, $p_{\mathrm{vi}} - p_{\mathrm{v}}$, as shown in Eq. (8). Therefore, analogous to the temperature effect, the length of the interface shrinks for smaller vapor pressure ratios, $p_{\mathrm{v}}/p_{\mathrm{v,eq}}$, due to higher flow rate in the thin film region. It is important to note that for this study, it is assumed that the liquid supply from the pore inlet to the interface is not constrained. To provide higher mass flow rates, it is expected that the pore inlet pressure

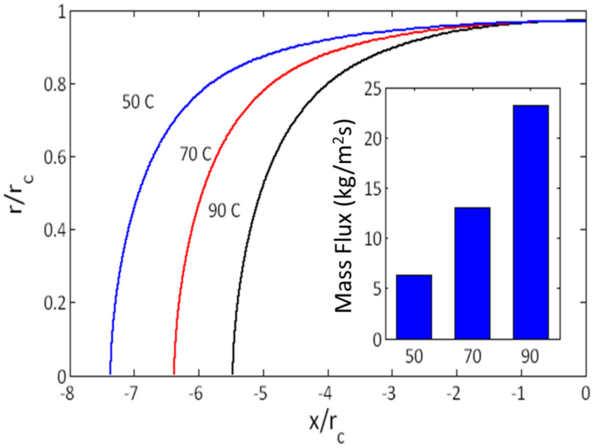

FIG. 7: Interface corresponding to $p_v/p_{v,eq} = 0.98$, $r_c = 50$ nm, and varying pore wall temperatures, $T_w = 50$, 70, and 90°C. The inset compares the average mass flux (kg/m^{2}s) at different wall temperatures (°C) (reprinted with permission from the American Chemical Society, Copyright 2011).[66]

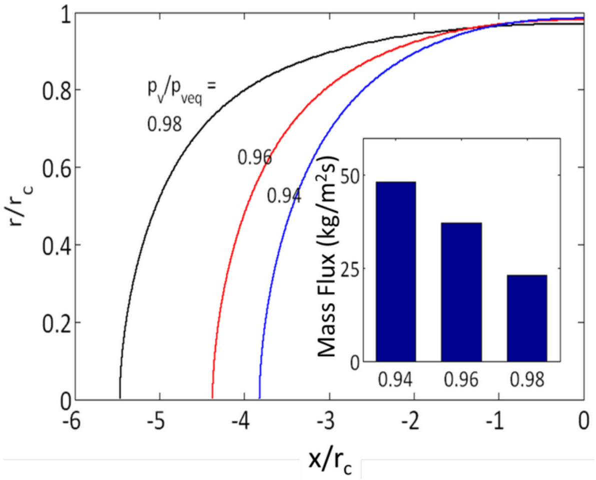

FIG. 8: Interface corresponding to $r_c = 50$ nm, $T_w = 90$°C, and varying the relative pressure in the ambient environment surrounding the meniscus, $p_v/p_{v,eq}$, of 0.98, 0.96, and 0.94. The inset compares the average mass flux (kg/m^{2}s) at different vapor pressures (reprinted with permission from the American Chemical Society, Copyright 2011).[66]

will be much higher at higher wall temperatures (and lower relative pressures) compared to the pore inlet pressure for lower wall temperatures (and higher relative pressures). Since the hydraulic resistance to supply liquid from the pore inlet to the interface is not considered, it is assumed that the liquid supply pressure at the pore inlet is consistent with the requirements of the overall evaporation rate, for the chosen geometry and operating conditions.

In summary, it is clear that a significant change in the shape of the interface is expected when electrostatic interactions exist in addition to van der Waals and capillary forces. The inclusion of thermocapillary stress does not yield measurable variation in interfacial characteristics for nanoscale capillaries, due to insufficient temperature gradient to induce stresses comparable to other driving forces. The effects of temperature and ambient vapor pressure on net rate of evaporation are shown to be analogous, wherein an increase in wall temperature, which enhances saturation pressure, or a decrease in the ambient vapor pressure, both result in an increase in the rate of evaporation from the interface. More importantly, the analysis highlights the possibility of achieving relatively high evaporation fluxes, if the nanopores are exposed to desirable ambient conditions. However, the ambient conditions are controlled by macroscale factors, which include the overall design and operation conditions of the device that enables thin film evaporation. The effects of these factors are discussed in more detail in the following section, which aims to relate global operational conditions to the performance at the pore level presented above.

4.2 Investigation of Gas-Assisted Evaporation using a Microscale Device

In a microscale device, a volatile liquid is supplied through a narrow channel bounded by a heating surface and a nanoporous alumina membrane (Fig. 9).[64] Being inherently hydrophilic, the nanoporous alumina membrane drives the liquid into the nanopores by capillary action against the viscous drag resisting flow through the pores. During evaporation, when the viscous drop exceeds the pressure differential driving liquid across the membrane, complete flooding of the membrane with liquid is prevented and the liquid-vapor interface is confined between the inlet and outlet of the membrane pores. Therefore, the membrane pores are generally only partly filled with the liquid, the rest being occupied by the air-vapor mixture. In this case, the rate of heat conduction across the liquid film is limited only by the liquid film thickness, which is governed by the separation of the membrane from the heater—a parameter that can be precisely controlled using micro-fabrication.[64] On the other hand, if the pores of the membrane are rendered hydrophobic with a suitable chemical coating, then the liquid-vapor interface will be pinned at the membrane pore

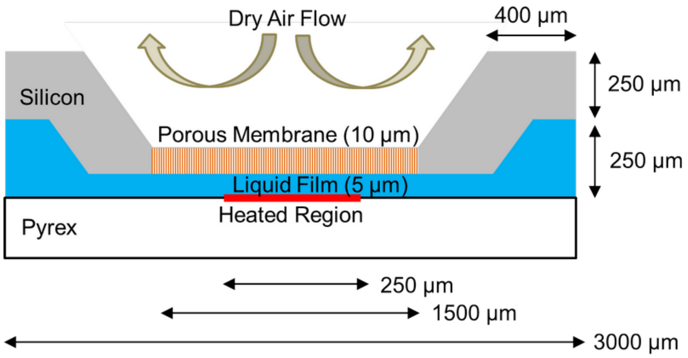

FIG. 9: A microscale device to enable thin film evaporation. The physical model illustrates key geometric parameters and boundary conditions for the analysis of heat and mass transfer.

inlet itself and the entire pore will then be occupied only by the air-vapor mixture. In such a case, a gas-phase mass transfer of vapor within the pores can become the rate-limiting process if the pore aspect ratio (length to diameter) is sufficiently large.[63]

In a hydrophilic membrane with cylindrical nanopores, due to variability in the location of the interface, liquid penetration into the pores can vary across the membrane. Consequently, for a hypothetical case, wherein a membrane pore is fully saturated with liquid, the interface is assumed to be pinned at the pore outlet, and the net vapor transport will be limited only by advection due to the air stream at the membrane outlet. On the other hand, for a membrane void of liquid, as in the case of a hydrophobic membrane, the vapor resulting from evaporation at the liquid-vapor interface must first diffuse through the pore before being removed via advection at the membrane outlet. The net vapor transport, in this case, is limited by diffusion as well as advection. Therefore, these two limiting cases set the overall range in the variation of net vapor transport, provided other operating conditions remain invariant.

When liquid is trapped within the membrane, evaporation occurs due to the heat generated at the heater, which may result in significant cooling. In addition, heat dissipation may also occur via convection due to the liquid flow across the heater. Clearly, if liquid flow is much larger than the overall rate of evaporation, capacitive heating of liquid between the porous membrane and the heated surface can be significant. When both capacitive and evaporative cooling are not significant, thermal spreading from the heater into the substrate will become prominent. Therefore, for any given liquid flow rate and heat generation at the surface, heat is dissipated due to evaporation, single-phase cooling, and spreading into the substrate. Determining the relative contributions of each mechanism is necessary to quantify the performance of gas-assisted evaporation using the microscale device. This is carried out via detailed computational and experimental analysis, as mentioned below.

4.2.1 *Computational Analysis of Heat and Mass Transfer during Thin Film Evaporation*

4.2.1.1 Equations Governing Fluid Flow and Heat Transfer at Device Level

For the device implementation illustrated in Fig. 9, the lateral dimensions of the heater and the membrane are much larger than the liquid film and membrane thicknesses. Because of the characteristic geometry of the flow cross section (liquid film thickness is much smaller than the channel depth), the out-of-plane fluid flow can be neglected in comparison to the in-plane fluid flow. Therefore, a 2D analysis of flow and heat transfer is carried out to predict the rate of heat dissipation from the heater for different operating conditions. Assuming a Newtonian fluid with constant density, ρ_l, and viscosity, μ_l, the steady flow of an incompressible liquid confined within the microchannel is governed by the following equations:

$$\nabla \cdot \bar{u}_l = 0 \tag{13}$$

$$\rho_l \bar{u}_l \cdot \nabla \bar{u}_l = -\nabla p_l + \mu_l \nabla^2 \bar{u}_l \tag{14}$$

where $\bar{u}_l$ and p_l represent the velocity and pressure of the liquid. The temperature distribution, T_l, within the liquid is given by the following equation, which assumes constant thermal conductivity, k_l, no internal heat generation, and negligible fluid compressibility effects

$$\rho_l c_{pl} \bar{u}_l \cdot \nabla T_l = k_l \nabla^2 T_l \tag{15}$$

It is to be noted that viscous dissipation due to flow in the narrow channel is also neglected, since the Brinkman number, $\mathrm{Br} = u_l^2 \, \mathrm{Pr}_l / c_{pl} \Delta T_l$, for the typical operating conditions is found to be negligibly small $\sim 10^{-9}$, where u_l represents the characteristic velocity scale. The temperature distributions in the Pyrex (T_p) and silicon (T_s) substrates (Fig. 9) are governed by the following equations, respectively:

$$k_p \nabla^2 T_p + \dot{q}_j''' = 0 \tag{16}$$

$$\nabla^2 T_s = 0 \tag{17}$$

where k_p is the thermal conductivity of Pyrex (assumed constant), and $\dot{q}_j'''$ represents volumetric heat generation within the substrate, generated by the heating element.

4.2.1.2 Evaporation within the Nanoporous Membrane

In order to determine the rate of evaporation inside the membrane pores, the vapor generated at the interface and its transport via diffusion and advection are quantified. The mass flux due to evaporation at the liquid-vapor interface surrounded by an air-vapor mixture is given by[94]

$$\dot{m}'' = \frac{2\hat{\sigma}}{2-\hat{\sigma}} \left(\frac{M_l}{2\pi \bar{R}} \right)^{1/2} p_{\mathrm{atm}} \left(\frac{X_{\mathrm{v,eq}}}{T_{\mathrm{li}}^{1/2}} - \frac{X_{\mathrm{vi}}}{T_{\mathrm{vi}}^{1/2}} \right) \tag{18}$$

where $X_{\mathrm{v,eq}}$ and X_{vi} are the equilibrium and interfacial mole fractions of vapor phase, defined as $p_{\mathrm{v,eq}}/p_{\mathrm{atm}}$ and $p_{\mathrm{vi}}/p_{\mathrm{atm}}$, respectively, where $p_{\mathrm{v,eq}}$ and p_{vi} denote the saturated vapor pressure at temperature T_{li} and the partial pressure of vapor in the air-vapor mixture in the immediate vicinity of the interface, respectively. T_{li} and T_{vi} represent the liquid and vapor temperatures in the immediate vicinity of the interface, respectively. M_l is the molecular weight of the evaporating liquid.

The rates of vapor transport by mass diffusion inside the membrane pores and by convection due to the sweep air at the membrane outlet are given by Eqs. (19) and (20), respectively

$$\dot{m}'' = \frac{D_k M_l p_{\mathrm{atm}}}{\delta_v \bar{R}} \left(\frac{X_{\mathrm{vi}}}{T_{\mathrm{vi}}} - \frac{X_{\mathrm{vo}}}{T_{\mathrm{vo}}} \right) \tag{19}$$

$$\dot{m}'' = \frac{h' M_l p_{\mathrm{atm}}}{\bar{R}} \left(\frac{X_{\mathrm{vo}}}{T_{\mathrm{vo}}} - \frac{X_{\mathrm{v}\infty}}{T_\infty} \right) \tag{20}$$

where X_{vo} and T_{vo} represent the mole fraction and temperature of the vapor phase at the membrane outlet, respectively; D_k represents the coefficient of combined Knudsen-molecular diffusion[63] across the length δ_v, which denotes the length of vapor column inside the pore; h' is the mass transfer coefficient for the transport of the vapor phase by air with far-field coolant vapor mole fraction $X_{\mathrm{v}\infty}$ and temperature T_∞. Based on the location of the interface inside the membrane pore, the possible values of δ_{v} are given by $0 \leq \delta_{\text{v}} \leq \delta_{\text{m}}$, where δ_{m} is the thickness of the membrane.

Assuming the vapor and membrane to be in local thermal equilibrium, the analysis can be simplified by neglecting the temperature difference $T_{\text{vi}} - T_{\text{vo}}$. This assumption is justified for thin ceramic (alumina) membranes ($\delta_{\text{m}} \sim 10^{-6}$ m) with thermal conductivity, $k_{\text{m}} \sim 10$ W/m K, since the temperature difference across the membrane is >0.1 K even for heat fluxes as high as 10^6 W/m^2. The liquid and vapor at the evaporating interface are assumed to be in thermal equilibrium, so that $T_{\text{li}} = T_{\text{vi}}$.[66] In other words, the difference in temperatures, $T_{\text{vi}} - T_{\text{vo}}$ and $T_{\text{li}} - T_{\text{vi}}$, are neglected whereas the differences in mole fractions, $X_{\text{vi}} - X_{\text{vo}}$ and $X_{\text{v,eq}} - X_{\text{vi}}$, are still considered significant. This simplification is justified because the temperature discontinuities are rendered negligible by the efficient thermal transport across the solid phase of the ceramic membrane. On the other hand, the differences in mole fractions are not negligible since vapor transport via diffusion is much less efficient.

Using a completely dry sweeping air, $X_{\text{v}\infty} = 0$, the overall rate of evaporation per unit area, after including the above-stated simplifications, is given by the following equation, which takes into account the available area for evaporation via the membrane porosity ε:

$$\dot{m}'' = \frac{p_{\text{atm}} M_{\text{l}} X_{\text{v,eq}} \varepsilon}{\bar{R} T_{\text{vi}}} \left(\frac{1}{(2-\hat{\sigma})/(2\hat{\sigma}) \left[2\pi M_{\text{l}}/\left(\bar{R} T_{\text{vi}}\right)\right]^{1/2} + \delta_{\text{v}}/D_{\text{k}} + 1/h'} \right) \tag{21}$$

Heat dissipation by evaporation within the thin porous membrane is approximated by a uniform volumetric heat sink term, $\dot{q}_{\text{m}}'''$, which is included in the energy conservation equation (22) for the membrane. The volumetric heat sink is derived from heat and mass transfer balance for the rate of evaporation inside the membrane as $\dot{q}_{\text{m}}''' = \dot{m}'' \hat{h}_{\text{fg}}/\delta_{\text{m}}$. This allows coupling between the modes of heat transfer occurring within and outside the membrane. It is to be noted that the use of a volumetric heat sink term as opposed to a uniform heat flux as a boundary condition in our analysis is pertinent to account for the variability in the location of the liquid-vapor interface inside the membrane. Furthermore, due to extremely small evaporation rates inside the membrane, convective heat transfer due to liquid and vapor flow in membrane pores is neglected in comparison to the latent heat of phase change and conduction across the solid structure of the membrane. The temperature distribution in the membrane can hence be given by

$$k_{\text{m}} \nabla^2 T_{\text{m}} + \dot{q}_{\text{m}}''' = 0 \tag{22}$$

where k_{m} represents the volumetrically averaged thermal conductivity of membrane, which is given by $(1-\varepsilon)\,k_{\text{al}} + \varepsilon k_{\text{l}}$ for a liquid-saturated membrane and by $(1-\varepsilon)\,k_{\text{al}} + \varepsilon k_{\text{v}}$ for a dry, vapor-saturated membrane; k_{al}, k_{l}, and k_{v} are the thermal conductivities of alumina, liquid, and vapor phases, respectively.

Computational analysis of the problem for the domain shown in Fig. 9 is carried out by solving the governing equations outlined above. For this study, the velocity at the liquid inlet is assumed uniform and assigned a value corresponding to the flow rates realized in the experimental study. The temperature of the liquid at the inlet is taken as the ambient condition. Since the liquid exiting the device is exposed to ambient conditions, a constant gage pressure is assigned at the liquid outlet. The heated surface denoted as "Heated Region" is analyzed as a thin layer with uniform volumetric heat generation. The other passive surfaces are assigned convective boundary conditions, with a heat transfer coefficient typical to natural convection. The sidewalls are assigned adiabatic boundary condition, representing walls that contribute negligibly to overall heat dissipation. The membrane surface is assigned convective boundary conditions with spatially varying heat transfer coefficients, which are determined from a separate computational analysis, which predicts the flow resulting from jet impingement of air within the confined space at the membrane outlet. Additional details on computational modeling and parameters are described in Ref. 67.

4.2.2 Experimental Study of Evaporation using a Microscale Device

4.2.2.1 Microscale Device for Investigation of Gas-Assisted Thin Film Evaporation

A microscale device, as shown in Fig. 10, fabricated using surface micromachining,[64] consists of three distinct layers. A device layer made on Pyrex constitutes an array of resistance temperature detectors (RTDs) and heaters. An array of 36 RTDs are fabricated on Pyrex substrate, with overall dimensions of 20 × 20 mm. Pyrex is chosen since it allows optical access to monitor evaporation and minimizes heat spreading due to its low thermal conductivity. Square hotspots of sizes 250, 500, and 750 μm are fabricated such that they are centrally located and surrounded by RTDs, which are densely packed at the center to record maximum temperature gradient when the hotspot is activated. The design of the hotspot and RTDs allows localized heating and sensing capability to provide an accurate thermal map during experimental testing. A second device layer facilitating fluid delivery to the hot surface is made using silicon. This layer includes microchannels and ports for delivery of liquid. More importantly, the device incorporates a nanoporous ceramic membrane, which is monolithically integrated to minimize contact resistances and accurately define the thickness of liquid film. The membrane confines a thin film over the heated surface and provides a passage for the vapor phase generated by evaporation to diffuse into the ambient as described before. A third intermediate adhesive layer bonds the Pyrex and

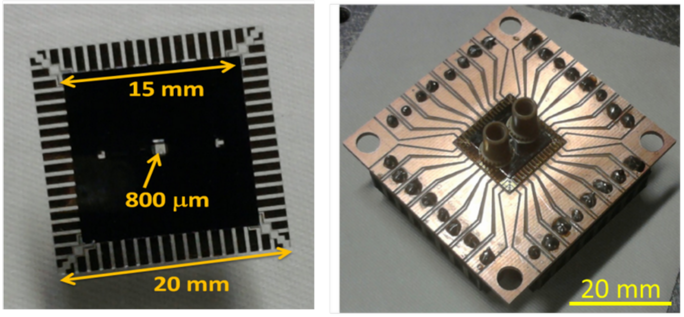

FIG. 10: A microscale device enabling study of thin film evaporation in confined environment, with a centrally located heater and a nanoporous alumina membrane (left), after interfacing with printed circuit board to communicate with external hardware (right) (reprinted with permission from IOP Publishing, Copyright 2010).[64]

silicon substrates. This layer also provides the necessary spacing between the silicon and Pyrex substrates, essentially defining the coolant film thickness between the membrane and the hotspot. A detailed description of the device fabrication process can be found in Refs. 64 and 65.

4.2.2.2 Experimental Procedure

The performance of dry air-assisted evaporation is measured at different combinations of liquid and airflow rates to determine the relative effect of single-phase convection and vapor advection, respectively. These effects are studied using devices with different characteristic dimensions of the film and membrane, while the heater dimensions in all test cases presented herein are 250×250 µm^2. The calibration of each RTD on the device is carried out prior to the experimental testing, to obtain a linear correlation of each RTD's resistance response to temperature.[64] The heater, activated using a DC power supply, causes Joule heating at the location of the heater where the resistance is highest. The supply of air and liquid are then initiated to enable evaporation and heat rejection to the ambient.

Jet impingement of air was implemented using nozzles of different internal diameters connected to a compressed air supply. The air supply line was connected in series with a flowmeter and a pressure transducer to measure the volumetric flow rate and gage pressure, respectively. The nozzle for air jet impingement was held using a positioning tool so that its separation from the heated surface and the angle of impingement could be controlled with precision. The results presented herein correspond to normal incidence of an air jet at different flow rates. The liquid used for thin film evaporation was deionized and deaerated water, which was circulated using a syringe pump capable of precisely delivering flow rates, and the temperature of the liquid at the inlet was measured using a calibrated thermocouple. The experiments were carried out at different air and liquid flow rates to determine the overall heat dissipation via evaporation and sensible cooling.

4.2.3 The Effect of Liquid Flow Rate

4.2.3.1 Computational Study of the Effect of Liquid Flow Rate

The net rate of evaporation and heat dissipated at different liquid flow rates for a fixed airflow is shown in Fig. 11. In order to determine the performance sensitivity to varying liquid rates, the location of the liquid-vapor interface is held constant at the membrane outlet, which eliminates vapor diffusion resistance within the membrane pores. Mathematically, this constraint is enforced by setting $\delta_{\mathrm{v}} = 0$. The effect of liquid flow is studied at a fixed average jet velocity of 30 m/s and a variable inlet velocity of the liquid between 0.001 and 0.004 m/s. This corresponds to Reynolds numbers for liquid flow, Re_{l}, ranging from 0.25 to 1, where the Reynolds number is calculated as $\mathrm{Re}_{\mathrm{l}} = u_{\mathrm{l}} d_{\mathrm{h}} / \nu_{\mathrm{l}}$. The hydraulic diameter for the thin film region is $d_{\mathrm{h}} \sim 10$ µm.

For relatively small flow rates ($\mathrm{Re}_{\mathrm{l}} \sim 0.1$), the heat dissipated due to conduction across the film thickness is more efficient than advection or capacitive heating of the liquid flowing between the membrane and the heated source. In this case, heat dissipation is primarily due to evaporation. As the temperature of the heat source approaches saturation condition, the

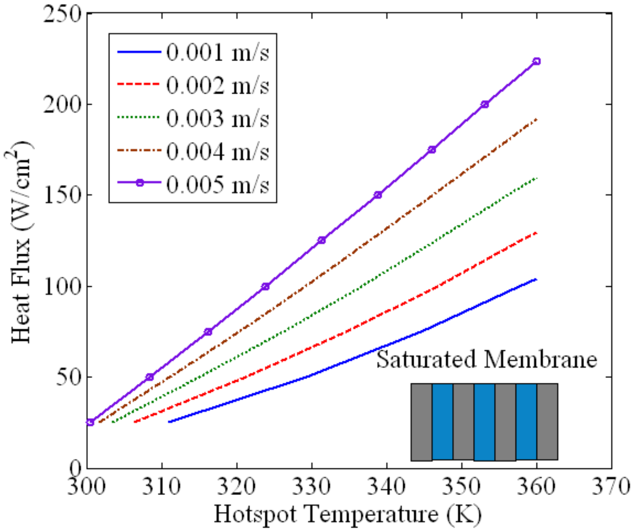

FIG. 11: Net heat flux dissipated versus heater temperature as a function of liquid flow rate ($\mathrm{Re}_l \sim 0.25$–1.25) for the microscale device illustrated in Fig. 10. The interfacial location is fixed at the membrane outlet, $\delta_v = 0$, which eliminates vapor diffusion resistance within the membrane pores, and the average velocity of air exiting the nozzle is 30 m/s corresponding to $\mathrm{Re}_j \sim 960$ (reprinted with permission Elsevier, Copyright 2013).[67]

rate of evaporation and cooling are both enhanced. For an inlet velocity of 0.001 m/s, the net heat flux dissipated at 360 K is 104 W/cm^2. With a quadruple increase in liquid flow rate, the rate of cooling can be enhanced to 192 W/cm^2, a twofold increase.

For these operating conditions, the relative contributions of evaporation, convection, and spreading to net heat dissipation from the heater are illustrated in Figs. 12(a)–12(c). Note that for most calculations, the location of the interface was fixed at the membrane outlet ($\delta_v = 0$), which eliminates the resistance to vapor diffusion, while considering only vapor advection resistance at the membrane outlet ($\sim 1/h'$). For performance comparison, we include the total heat flux achievable when the vapor advection resistance is eliminated ($h' \to \infty$), while considering the maximum resistance to vapor diffusion (δ_v/D_k, where $\delta_v = \delta_m$). This allows comparing the effect of vapor diffusion within pores to vapor advection at the membrane outlet.

At a low liquid flow rate ($\mathrm{Re}_l \sim 0.25$), evaporation and sensible cooling contribute about 90% and 7% of net heat dissipation, respectively, and the remaining 3% is attributed to spreading in the substrate. For a quadruple increase in liquid flow rate ($\mathrm{Re}_l \sim 1$), the relative contribution of single-phase convection is ~34%, which is still lower than the contribution of evaporation of ~64%. The pressure drop to pump liquid across the thin film region for inlet velocities of 0.001 and 0.004 m/s is 6.1 and 24.7 kPa, respectively, which translates to a 16-fold increase in pumping power for a quadruple increase in liquid flow rate. At a significantly higher liquid flow rate, $\mathrm{Re}_l = 2.5$, sensible cooling evidently supersedes contribution from evaporation [Fig. 12(c)]. The result demonstrates the enhancement in net heat flux due to a higher contribution of single-phase convection at higher liquid flow

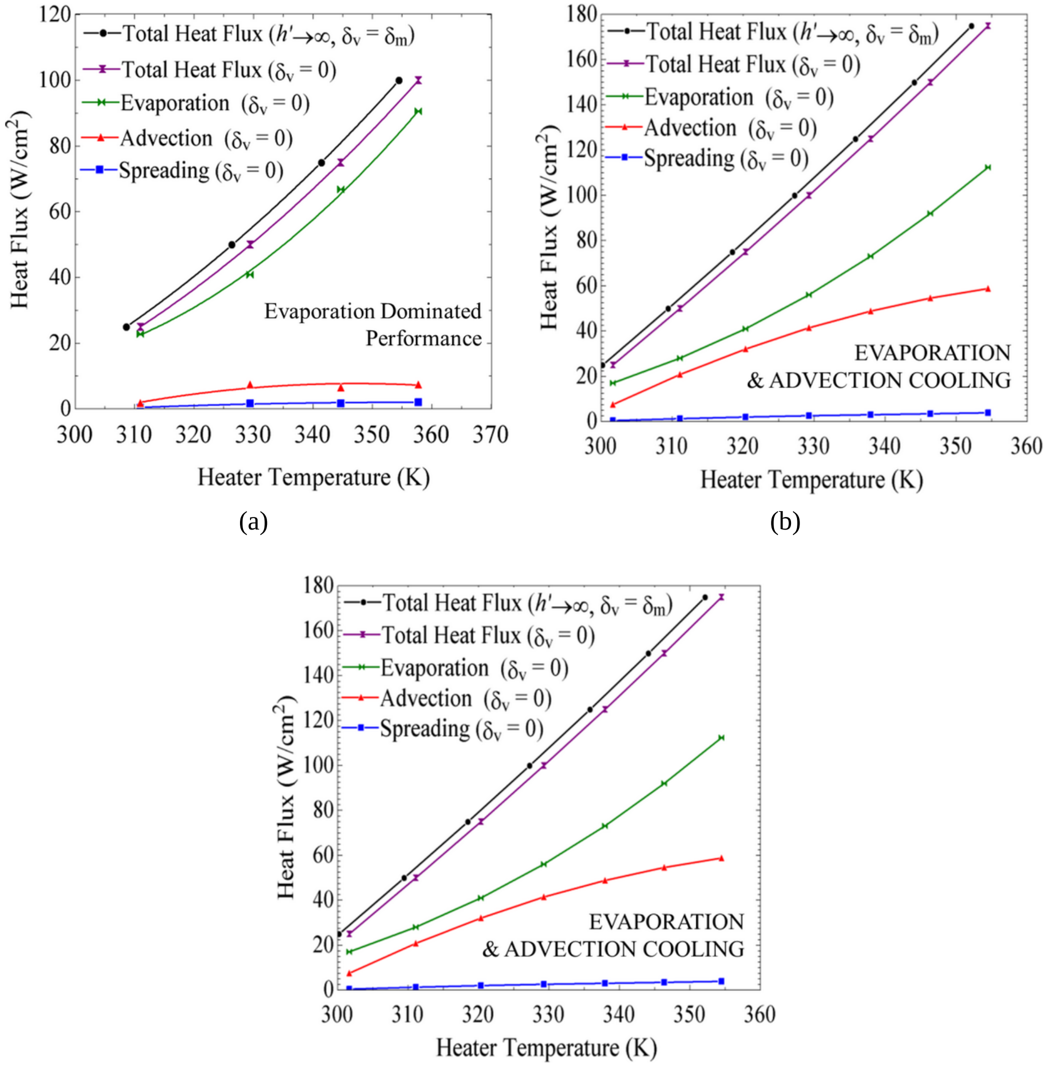

(a) (b)

(c)

FIG. 12: Relative contributions of evaporation, sensible cooling, and substrate spreading to the net heat dissipation from the heated surface. The coolant velocity was maintained at (a) 0.001 and (b) 0.004 m/s, and (c) 0.01 m/s, corresponding to $\mathrm{Re}_l = 0.25$, 1, and 2.5, respectively. The air velocity was fixed at 30 m/s, corresponding to $\mathrm{Re}_j \sim 960$, based on jet diameter. Interface locations at the membrane outlet and inlet are denoted by $\delta_v = 0$ and $\delta_v = \delta_m$, respectively h' denotes the mass transfer coefficient (reprinted with permission Elsevier, Copyright 2013).[67]

rates. In applications requiring cooling of small heat sources, the utilization of enhanced advection is viable since the net pumping power is practically achievable. However, for larger heat sources and applications such as membrane distillation, it is necessary to induce significant evaporation and rely less on capacitive cooling, which requires maximizing the rate of vapor transport from the liquid-vapor interface.

4.2.3.2 Experimental Study of the Effect of Liquid Flow Rate

A microscale device with film and membrane thicknesses of 15 and 10 μm, respectively, was tested at different liquid flow rates, corresponding to inlet velocities of the liquid between 0.01 and 0.03 m/s. The air velocity was fixed at 65 m/s, for normally impinging dry nitrogen gas from a circular nozzle, 1000 μm in diameter, placed 1500 μm from the membrane surface with lateral dimensions of 800 × 800 μm.

The net heat flux recorded during the experiments, as a function of temperature of the surface, is compared with the computational predictions for the matching operating conditions. The computational results have been evaluated assuming a membrane fully saturated with liquid, $\delta_v = 0$. The inclusion of vapor diffusion resistance in the analysis introduces a negligible variation in the predicted values of device performance due to the dominance of sensible cooling. The results obtained from computational analysis for different liquid flow rates are shown along with experimental observation in Fig. 13. It is apparent that by combining evaporation and sensible cooling modes, heat flux in excess of 500 W/cm^2 is realizable with heater temperatures under 360 K. In this case, with $Re_l > 2.5$, the contribution of sensible cooling is in excess of 65%, as already shown in Fig. 12(c).

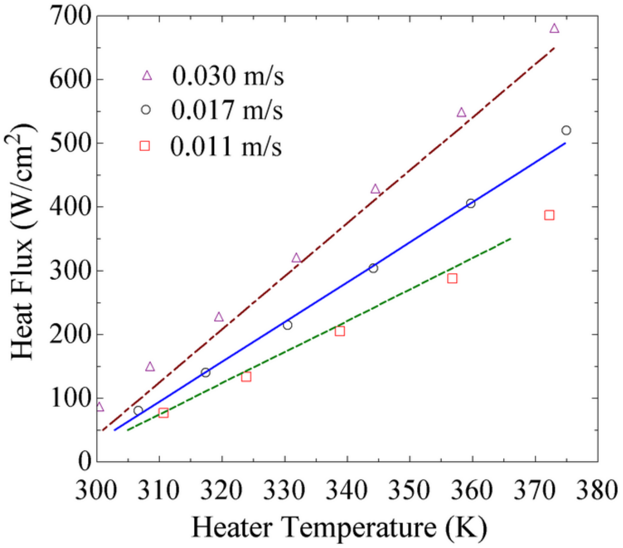

FIG. 13: Net heat flux dissipated at the heater for liquid flow rates much larger than the rate of evaporation ($Re_l > 2.5$). The sweeping air velocity was held constant at 65 m/s, corresponding to $Re_j \sim 4300$ based on the air jet diameter at 20°C. The computational simulations for performance characterization under similar operating conditions (shown by dotted and continuous lines) assume an interfacial location pinned at the membrane outlet ($\delta_v = 0$) (reprinted with permission Elsevier, Copyright 2013).[67]

4.2.4 The Effect of Airflow Rate

4.2.4.1 Computational Study of the Effect of the Airflow Rate

For the microscale device illustrated in Fig. 9, the net heat flux dissipated at different flow rates for air jet impingement is shown in Fig. 14. The variation in airflow rate at the membrane outlet corresponds to jet Reynolds number, $\mathrm{Re_j}$, between 320 and 1600, based on the nozzle diameter, evaluated at 20°C. Contrary to the effect observed by increasing the liquid flow rate, the incremental change in performance is not as significant for a commensurate increase in airflow rate. In other words, a fivefold increase in air velocity from 10 to 50 m/s demonstrates an enhancement of only 20% in the net heat dissipation. In this case, since the contribution from the sensible heating of the liquid remains invariant, the enhancement in rate of evaporation due to the variation in vapor advection can be determined. With a fivefold increase in the flow rate, a 38% increase in the contribution of evaporation to net heat dissipation is observed, although for these conditions the heat and mass transfer coefficients at the stagnation zone are enhanced 2.5 times.

Clearly, the same extent of improvement in evaporative cooling is not observed, which can be explained based on the combined effect of mass transfer coefficient, vapor pressure, and interfacial temperature across the membrane. In a membrane fully saturated with the evaporating liquid, the interfacial resistance to evaporation per unit area is negligible in comparison to the vapor advection resistance. Therefore, from Eq. (21) it is clear that the rate of evaporation varies as $h'\left(p_{\mathrm{atm}}X_{\mathrm{v,eq}}\right)/T_{\mathrm{vi}} = h'p_{\mathrm{v,eq}}/T_{\mathrm{vi}}$, where the expression within the parenthesis denotes saturation pressure $p_{\mathrm{v,eq}}$ at temperature T_{vi}. Although the mass transfer coefficient, h', increases by 150%, the increase in the average value of $h'p_{\mathrm{v,eq}}/T_{\mathrm{vi}}$

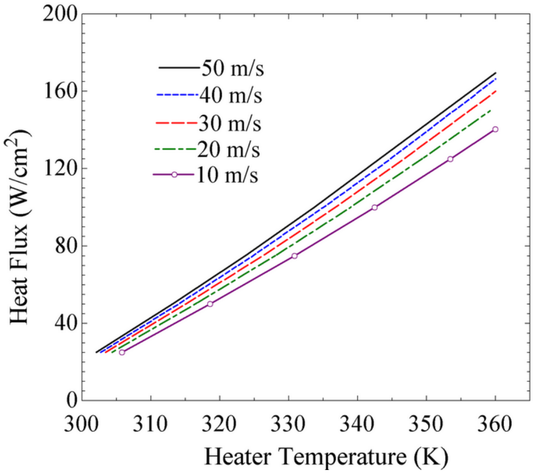

FIG. 14: The net heat flux dissipated versus heater temperature as a function of average air jet velocity at the nozzle exit. The sweeping air velocity was varied between 10 and 50 m/s, corresponding to $\mathrm{Re_j}$ between 320 and 1600, based on the air jet diameter at 20°C. The inlet liquid coolant velocity was held constant at 0.003 m/s corresponding to $\mathrm{Re_l} = 0.75$. The computational simulations assume an interface pinned at the membrane outlet ($\delta_v = 0$) (reprinted with permission Elsevier, Copyright 2013).[67]

over the surface of the membrane is only 38%, which matches the observed increase in the net evaporative heat flux. Although enhanced mass transport can improve vapor advection, a consequent decrease in the interfacial temperature and vapor pressure can depreciate the net rate of evaporation. The combination of the three factors determines the net heat dissipation. In order to improve the net rate of evaporation, it is essential to utilize a liquid with a large evaporation potential, $p_{\text{v,eq}}/T_{\text{vi}}$, and a highly efficient vapor advection mechanism providing a large mass transfer coefficient, h'.

4.2.4.2 Experimental Study of the Effect of Airflow Rate

For the device features illustrated in Fig. 9, the inlet velocity for the liquid was set at 0.004 m/s, $\text{Re}_\text{l} = 1$, and the device performance was studied for an average air jet velocity of 30 m/s and 50 m/s from a normally incident air jet of diameter 500 μm, anchored at 500 μm from the membrane surface. The net heat flux dissipated at the heated surface is plotted as a function of heater temperature in Fig. 15. Corresponding to these operating conditions, the heat flux was also predicted using the computational analysis for interface positions coinciding with the membrane inlet $(\delta_\text{v} = \delta_\text{m})$ and the outlet $(\delta_\text{v} = 0)$. The predicted heat flux corresponding to interface locations at membrane inlet and outlet are shown in Fig. 15. For both interface locations, with the sweep air velocities corresponding to 30 and 50 m/s, the net heat flux dissipated from the heated surface at 360 K was found to be close to 180 W/cm^2. The net contributions of evaporation and capacitive cooling are predicted as 65% and 35%, respectively, with negligible spreading into the substrate.

A comparison of experimental results with computational predictions demonstrates an interesting observation. When the liquid flow rate at the inlet is held constant, the net rate of

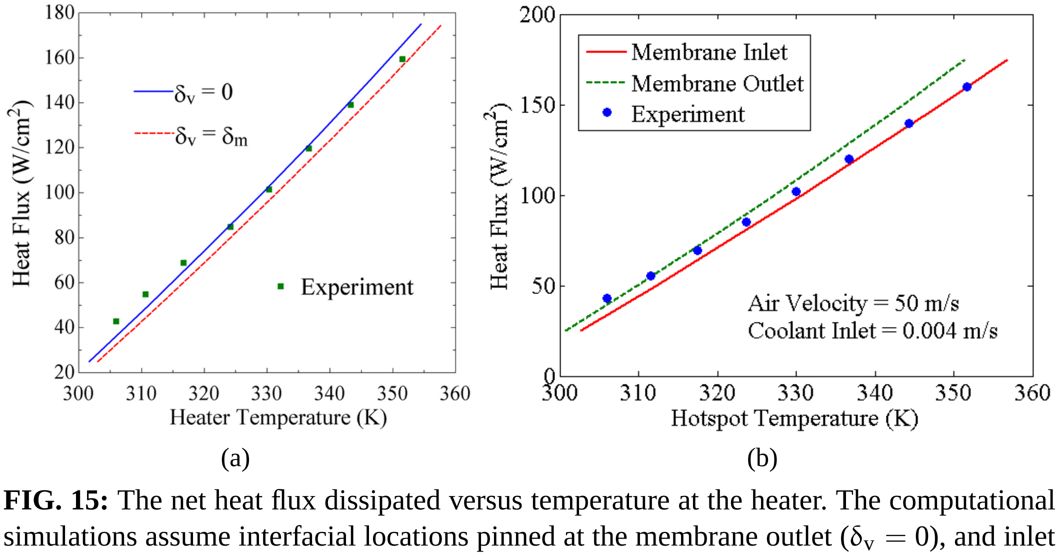

(a) (b)

FIG. 15: The net heat flux dissipated versus temperature at the heater. The computational simulations assume interfacial locations pinned at the membrane outlet $(\delta_\text{v} = 0)$, and inlet $(\delta_\text{v} = \delta_\text{m})$. The average liquid velocity is 0.004 m/s, corresponding to $\text{Re}_\text{l} = 1$ and the air jet velocity is (a) 30 m/s, $\text{Re}_\text{j} = 960$ and (b) 50 m/s, $\text{Re}_\text{j} = 1600$ (reprinted with permission Elsevier, Copyright 2013).[67]

evaporation from the membrane is smaller at lower heat fluxes and it increases as the heater temperature rises with higher heat fluxes. At lower heat fluxes, the experimental observations match well with computational predictions corresponding to the interface pinned at the membrane outlet ($\delta_v = 0$). On the other hand, at higher heat fluxes, they match the predicted heat flux corresponding to the interface located at the membrane inlet $(\delta_v = \delta_m)$. This variation is indicative of the system self-adjusting its overall thermal resistance to match the heat flux supplied at the heated surface.

4.2.5 Resistances Limiting Heat and Mass Transfer

Based on the net heat dissipated by evaporation alone and the temperature variation across the heated surface and membrane inlet, the thermal resistances to heat conduction across the liquid film and vapor advection at the membrane outlet are calculated for the device illustrated in Fig. 9. Figures 16(a) and 16(b) compare the net thermal resistance to conduction and advection resistance, for different liquid and airflow rates, respectively. The net thermal resistance decreases for a higher liquid and airflow rate. It is to be noted that the decrease in net resistance at a higher liquid and airflow rate is mainly due to a corresponding decrease in thermal resistance due to liquid and air convection, respectively. More importantly, the thermal resistance to convection across the liquid film and vapor advection at the membrane outlet are comparable. Therefore, the overall rate of evaporation can be increased by decreasing the film thickness or utilizing a highly conductive

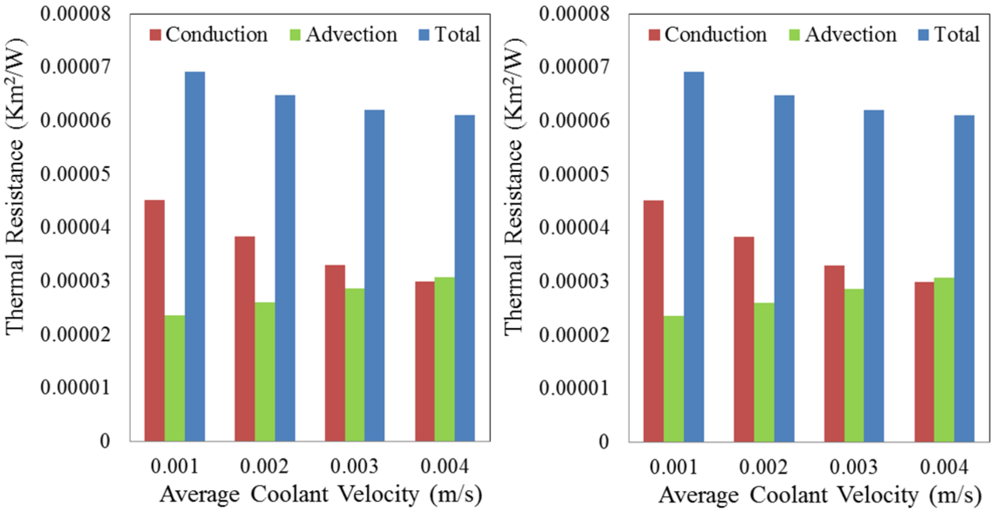

(a) (b)

FIG. 16: Thermal resistance corresponding to conduction and vapor advection for (a) a fixed air jet velocity of 30 m/s, $Re_j = 960$ and variable liquid inlet velocities corresponding to Re_l between 0.25 and 1.25, and (b) a fixed liquid inlet velocity of 0.003 m/s, $Re_l = 0.75$, and variable air jet velocities, corresponding to Re_j between 320 and 1280. The computational simulations assume an interfacial location pinned at the membrane outlet ($\delta_v = 0$) (reprinted with permission Elsevier, Copyright 2013).[67]

porous structure within the thin film region along with a more efficient vapor advection mechanism. While the film thickness can be easily controlled by altering the fabrication process,[64] it is however more challenging to enhance the overall rate of vapor advection beyond that achievable using jet impingement of dry air. For a cooling mechanism based on evaporation wherein the thickness of the liquid film can be easily minimized, the rate of vapor advection eventually limits the net heat flux and distillate throughput.

4.2.6 *Performance Improvement through Membrane Upstream Placement and Air-Side Pressure Reduction*

A route to improvement of this already highly successful cooling scheme can be envisioned by recognizing that the conditions under which the best performance has been demonstrated can be classified as mass transfer limited local cooling of the forced convection liquid stream. The degree of local cooling of the liquid can be improved through reduction of the resistance to mass transfer, which is possible through the conceptually simple and straightforward expedient of reducing the gas pressure, which increases the diffusion coefficient of water vapor in the gas phase. The effectiveness of the reduction of liquid temperature on raising the heat flux can be improved by positioning the membrane so that the thermal perturbation has completely propagated across the micro-constriction prior to being advected past the leading edge of the hotspot. These ideas are pictorially represented in Fig. 17.

We investigated the potential impact of the patch upstream placement and use of vacuum-driven gas jets on the air side of the membrane to lower pressure and increase the rate of water vapor removal through simulations in the CFD code FLUENT. We use a 2D simulation to quantitatively predict the degree to which the performance of the current device might be improved. The simplified geometry for the simulations is depicted in Fig. 18. We use a simplified the membrane treatment, using a specified heat flux boundary condition

$$q'' = h_{\mathrm{T}} \left(T - T_{\mathrm{air}}\right) + h' h_{\mathrm{fg}} \rho_{\mathrm{sat}} \tag{23}$$

where the heat transfer coefficient, h_{T}, and the mass transfer coefficient, h', are obtained from their values at a reference state, and we have assumed that the water vapor density in the injected air stream is negligible. The variation of the heat transfer coefficient with pressure is obtained from $h_{\mathrm{T}} = h_{\mathrm{T,ref}} \left(P/P_{\mathrm{ref}}\right)^{n}$, where the variation with pressure arises from the effect on density, and $n$is a number between 0.5 and 0.9. The mass transfer coefficient is obtained from $h' = h'_{\mathrm{ref}} \left(P/P_{\mathrm{ref}}\right)^{1-n}$ where the enhancement in mass transfer coefficient comes from the increase in diffusion coefficient with decreasing pressure. The mass transfer coefficient at the reference state is obtained using $h'_{\mathrm{ref}} \approx h_{\mathrm{T,ref}} \sqrt{D/(k\rho c) \,|_{\mathrm{air,ref}}}$.

To find the saturation density of the vapor, we use the Clausius-Clapeyron relationship combined with the ideal gas equation of state,

$$\rho_{\mathrm{sat}} \left(T\right) \approx \rho_{\mathrm{sat}} \left(T_{\mathrm{ref}}\right) \frac{T}{T_{\mathrm{ref}}} \exp \left[\frac{h_{\mathrm{fg}} \left(T\right)}{R} \left(\frac{1}{T_{\mathrm{ref}}} - \frac{1}{T}\right)\right] \tag{24}$$

Finally, the variation of the latent heat of vaporization with interface temperature is obtained using a linearization, $h_{\mathrm{fg}} \left(T\right) \approx h_{\mathrm{fg}} \left(T_{\mathrm{ref}}\right) + \left(dh_{\mathrm{lv}}/dT\right)|_{T_{\mathrm{ref}}} \left(T - T_{\mathrm{ref}}\right)$.

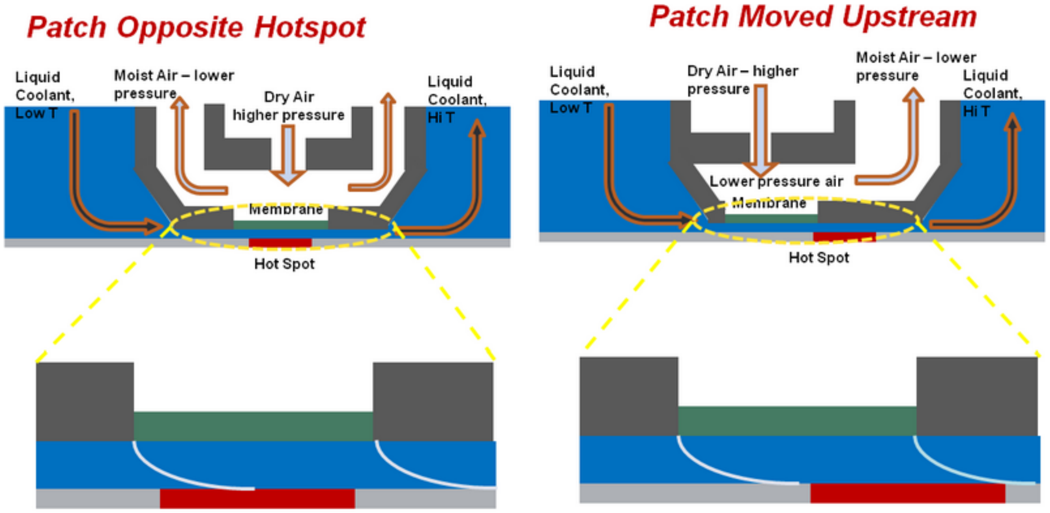

FIG. 17: The cooling capacity of the evaporation membrane can be improved through reduction of the resistance to mass transfer on the air side. When the liquid-side thermal Peclet number is greater than unity, patch location optimization is linked directly to thermal boundary layer growth, indicated in the figure with white curves. With the patch directly opposite the hotspot, the leading edge of the hotspot sees no cooling effect, while much of the cooling effect is wasted. With the patch upstream of the hotspot, the impact is enhanced in spite of a lower net rate of evaporation (due to lower mean liquid temperature at the membrane). Simulations indicate that through the combined effect of reduced gas-phase pressure and patch placement optimization the effect of the evaporative membrane on forced convection cooling is increased by 300%.

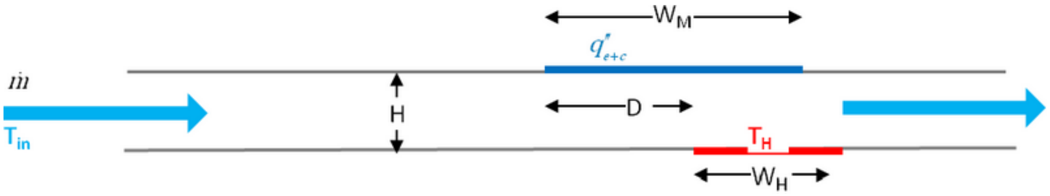

FIG. 18: Simplified geometry for simulations to quantify potential improvement due to patch placement and increased evaporation.

FLUENT simulations were performed for water using the boundary condition in Eq. (23), with $T_{\text{air}} = T_{\text{ref}} =$ 25°C, $h_{\text{T,ref}} =$ 6000 W/(m^{2}K), mean inlet velocity of 0.4 m/s (corresponding to a Peclet number of 42), and inlet temperature of 25°C. The geometric parameters include the hotspot width, $W_{\text{H}} =$ 250 μm, microchannel height, $H =$ 15 μm, membrane width, $W_{\text{M}} =$ 750 μm, and the membrane leading edge offset, D, varying from 250 μm (membrane centered above hotspot) to 750 μm. A pressure effect exponent, $n =$ 0.5, was utilized. The hotspot uniform heat flux was increased in each simulation to find the maximum heat flux for which the maximum local hotspot temperature did not exceed 85°C.

A comparison of four forced convection cases with (i) no evaporative cooling applied, (ii) evaporative cooling at $P_{\text{ref}} = P_{\text{atm}}$ and $W_{\text{H}} = 250$ µm, (iii) evaporative cooling at $P_{\text{ref}} = P_{\text{atm}}/10$ and $W_{\text{H}} = 250$ µm, and, (iv) evaporative cooling at $P_{\text{ref}} = P_{\text{atm}}/10$ and $W_{\text{H}} = 750$ µm was made. For the four cases, the maximum achievable hotspot heat fluxes were (i) 4 MW/m^2, (ii) 4.3 MW/m^2, (iii) 4.65 MW/m^2, and (iv) 4.9 MW/m^2. Thus, in the regime of advection dominated cooling, where the application of the evaporative cooler results in only a moderate ($<$10%) enhancement over simple forced advection cooling, the benefit of the evaporative cooler can be dramatically increased. This increase can be a factor of 3, through implementation of the combined strategy of mass removal enhancement via air-side pressure reduction, and the upstream placement of the cooling patch to ensure that the effect of reduced bulk liquid temperature is seen by the entirety of the hotspot.

5. SUMMARY AND FUTURE WORK

Evaporation plays a critical role in nature and myriad industrial applications such as water desalination, catalysis and fuel cells, combustion and fire extinguishing, and heating and air-conditioning. In particular, heat dissipation via evaporation has been extensively studied and demonstrated in various electronic cooling strategies. These take advantage of evaporation of water and dielectric liquids via shear-driven liquid flow, spray and mist, micro- and nanostructures, electrowetting, and chemically functionalized surfaces to achieve relatively high cooling performances. However, the problem of dissipating heat from electronic devices has grown from being an important concern to becoming a widely recognized bottleneck limiting further progress of high-performance microelectronics. This chapter describes how gas-assisted evaporation can be leveraged to address these thermal demands in electronics.

For high-power electronics, a hybrid approach, using on-demand and spatially controlled droplet impingement in combination with conventional forced air cooling, enables evaporative enhancement in the performance of conventional air-cooled heat sinks. The experimentally observed gains in performance, including a drop in the heated surface temperature by $\sim$15% and $\sim$50% increase in power dissipation, have been demonstrated as compared to an equivalent air-only cooled heat sink. This motivates further in-depth studies to improve performance of the hybrid thermal management scheme, including (i) better design of film spreading finned surface, (ii) matching the flow rates of air and mist to achieve complete evaporation with neither flooding nor dry-out of the heat transfer surfaces, (iii) optimization of size and speed of ejected droplets and mist delivery duty cycle, to minimize convective heat and mass transfer resistance across the liquid film created by impinging droplets, and (iv) the development of an on-demand control system capable of dynamically adjusting mist delivery to desired domains of the heat sink that experience an increase in the dissipated power or surface temperature.

A new approach to evaporative cooling using microscopically thin liquid films is also presented to address emerging thermal challenges in current and next-generation electronics. Membrane-enabled gas-assisted evaporation relies on capillary confinement of liquid using nanoporous membranes rather than hydrodynamics to define the film thickness. Consequently, it allows for precise control of the liquid film, making it as thin as possible to minimize the thermal conduction resistance. At the same time, the overall mass transfer of vapor phase is maximized by using a dry sweeping gas. The operation and performance characterization of a microscale device leveraging gas-assisted thin film evaporation provided heat fluxes >600 W/cm^2, and overall heat transfer coefficients >90 kW/m^2 K. A detailed theoretical analysis of interfacial transport during evaporation of water confined within nanopores was carried out, highlighting the advantage of using thin film evaporation over single-phase cooling. In addition, a detailed characterization of the microscale device also reveals the presence of multimode heat transfer to remove extremely high heat fluxes. It is clear that membrane-enabled thin film evaporation promises even higher cooling performance. However, this requires further research in several directions, some of which are mentioned below.

The current understanding of interfacial transport inside nano-capillaries will be significantly enhanced if the following factors are elucidated.

1. The disjoining pressure arising due to the electrostatic interactions is calculated using Langmuir's equation for thin films of a dilute electrolyte on a surface of high intrinsic electric potential. In order to include electrostatic interactions between various surface-liquid pairs, an alternative and more accurate analysis for a broader range of ionic strengths of electrolytes needs to be carried out for the free charge and electric potential distribution in polar solvents. The electrostatic disjoining pressure can then be obtained from these distributions and incorporated into the analysis.

2. The current study demonstrates interfacial characteristics and transport when water wets the surface of the membrane pores. Since the use of a hydrophobic membrane is an essential alternative for implementing this cooling mechanism, a theoretical analysis of interfacial transport of water confined by nonwetting pores is essential, and is yet to be reported in the literature.

3. In a highly curved meniscus within a nanopore, a liquid-vapor interface can "see itself." Consequently, vapor emitted from one region of the interface can directly condense onto another region of the interface. This effect of vapor re-condensation, arising purely due to geometric effects, needs to be accounted.

4. Evaporation flux from an interface is calculated using the Shrage equation derived from kinetic theory. The application of classical kinetic theory, with an accommodation coefficient of unity, requires further review, especially for the analysis of evaporation within nanoscale geometries. A recent publication discusses some of these aspects in detail.[105] In typical experiments characterizing evaporation, macroscale effects often dominate, resulting in low heat fluxes. Consequently, local effects arising from near-interface transport are not critical. However, as heat fluxes approach the theoretical sonic limit for vapor removal, as deemed necessary in future high-power electronics, the local effects become prominent. As a result, a detailed understanding of non-continuum transport and deviation from classical kinetic theory requires further elucidation.

REFERENCES

1. Meindersma, G. W., Guijt, C. M., and de Haan,A. B., Desalination and Water Recycling by Air Gap Membrane Distillation, *Desalination*, vol. 187, no. 1-3, pp. 291–301, 2006.
2. Nguyen, T. V., A Water and Heat Management Model for Proton-Exchange-Membrane Fuel Cells, *J. Electrochem. Soc.*, vol. 140, no. 8, p. 2178, 1993.
3. Wang, Y. and Wang, C.-Y., A Nonisothermal, Two-Phase Model for Polymer Electrolyte Fuel Cells, *J. Electrochem. Soc.*, vol. 153, no. 6, pp. A1193–A1200, 2006.
4. Grant, G., Brenton, J., and Drysdale, D., Fire Suppression by Water Sprays, *Prog. Energy Combust. Sci.*, vol. 26, pp. 79–130, 2000.
5. Sazhin, S. S., Advanced Models of Fuel Droplet Heating and Evaporation, *Prog. Energy Combust. Sci.*, vol. 32, no. 2, pp. 162–214, 2006.
6. Cavaliere, A. and de Joannon, M., Mild Combustion, *Prog. Energy Combust. Sci.*, vol. 30, pp. 329–366, 2004.
7. Maqua, C., Castanet, G., and Lemoine, F., Bicomponent Droplets Evaporation: Temperature Measurements and Modelling, *Fuel*, vol. 87, no. 13-14, pp. 2932–2942, 2008.
8. Asdrubali, F., A Scale Model to Evaluate Water Evaporation from Indoor Swimming Pools, *Energy Build.*, vol. 41, no. 3, pp. 311–319, 2009.
9. Shah, M. M., Prediction of Evaporation from Occupied Indoor Swimming Pools, *Energy Build.*, vol. 35, pp. 707–713, 2003.
10. Prevo, B. G. and Velev, O. D., Controlled, Rapid Deposition of Structured Coatings from Micro- and Nanoparticle Suspensions, *Langmuir*, vol. 20, no. 6, pp. 2099–2107, 2004.
11. Bigioni, T. P., Lin, X., Nguyen, T. T., Corwin, E. I., Witten, T. A., and Jaeger, H. M., Kinetically Driven Self Assembly of Highly Ordered Nanoparticle Monolayers, *Nat. Mater.*, vol. 5, no. 4, pp. 265–270, 2006.
12. Shimmin, R. G., Dimauro, A. J., and Braun, P. V., Slow Vertical Deposition of Colloidal Crystals: A Langmuir–Blodgett Process, *Langmuir*, vol. 22, no. 15, pp. 6507–6513, 2006.
13. Sau, T. K., Murphy, C. J., and Carolina, S., Self-Assembly Patterns Formed upon Solvent Evaporation of Aqueous Cetyltrimethylammonium Bromide-Coated Gold Nanoparticles of Various Shapes, *Langmuir*, vol. 21, no. 7, pp. 2923–2929, 2005.
14. Azar, K., The History of Power Dissipation, *Electron. Cooling*, vol. 6, no. 1, pp. 42–50, 2000.
15. Bar-Cohen, A. and Iyengar, M., Design and Optimization of Air-Cooled Heat Sinks for Sustainable Development, *IEEE Trans. Compon. Packag. Technol.*, vol. 25, no. 4, pp. 584–591, 2002.
16. Kandlikar, S. G. and Grande, W. J., Evolution of Microchannel Flow Passages–Thermohydraulic Performance and Fabrication Technology, *Heat Transfer Eng.*, vol. 24, no. 1, pp. 3–17, 2003.
17. Kandlikar, S. G. and Grande, W. J., Evaluation of Single Phase Flow in Microchannels for High Heat Flux Chip Cooling—Thermohydraulic Performance Enhancement and Fabrication Technology, *Heat Transfer Eng.*, vol. 25, no. 8, pp. 5–16, 2004.
18. Dhir, V., Boiling Heat Transfer, *Annu. Rev. Fluid Mech.*, vol. 30, no. 1, pp. 365–401, 1998.
19. Thome, J. R., Boiling in Microchannels: A Review of Experiment and Theory, *Int. J. Heat Fluid Flow*, vol. 25, no. 2, pp. 128–139, 2004.

20. Kabov, O. A., Zaitsev, D. V., Cheverda, V. V., and Bar-Cohen, A., Evaporation and Flow Dynamics of Thin, Shear-Driven Liquid Films in Microgap Channels, *Exp. Thermal Fluid Sci.*, vol. 35, no. 5, pp. 825–831, 2011.

21. Amon, C. H., Yao, S. C., Wu, C. F. and Hsieh, C. C., Microelectromechanical System-Based Evaporative Thermal Management of High Heat Flux Electronics, *J. Heat Transfer*, vol. 127, no. 1, pp. 66–75, 2005.

22. Coursey, J. S., Kim, J., and Kiger, K. T., Spray Cooling of High Aspect Ratio Open Microchannels, *J. Heat Transfer*, vol. 129, no. 8, pp. 1052–1059, 2007.

23. Hsieh, C.-C. and Yao, S.-C., Evaporative Heat Transfer Characteristics of a Water Spray on Micro-Structured Silicon Surfaces, *Int. J. Heat Mass Transfer*, vol. 49, no. 5-6, pp. 962–974, 2006.

24. Myers, S. H. and Smith, A. N., Demonstration of Combined Spray and Evaporative Cooling of an Electromagnetic Railgun, *IEEE 14th Symposium on Electromagnetic Launch Technology*, vol. 45, no. 1, pp. 396–401, 2008.

25. Wang, H.-C. and Mamishev, A. V., Optimization Methodology for Electrospray Evaporative Cooling Chambers, *J. Electrostat.*, vol. 70, no. 4, pp. 384–392, 2012.

26. Wang, H.-C. and Mamishev, A. V., Heat Transfer Correlation Models for Electrospray Evaporative Cooling Chambers of Different Geometry Types, *Appl. Thermal Eng.*, vol. 40, pp. 91–101, 2012.

27. Bodla, K. K., Weibel, J. A., and Garimella, S. V., Advances in Fluid and Thermal Transport Property Analysis and Design of Sintered Porous Wick Microstructures, *J. Heat Transfer*, vol. 135, no. 6, 061202, 2013.

28. Nam, Y., Sharratt, S., Cha, G., and Sungtaek, Ju., Y., Characterization and Modeling of the Heat Transfer Performance of Nanostructured Cu Micropost Wicks, *J. Heat Transfer*, vol. 133, no. 10, 101502, 2011.

29. Warrier, G. R., Kim, C.-J., and Sungtaek Ju, Y., Microchannel Cooling Device with Perforated Side Walls: Design and Modeling, *Int. J. Heat Mass Transfer*, vol. 68, pp. 174–183, 2014.

30. Sun, Z., Chen, X., and Qiu, H., Experimental Investigation of a Novel Asymmetric Heat Spreader with Nanostructure Surfaces, *Exp. Thermal Fluid Sci.*, vol. 52, pp. 197–204, 2014.

31. Cheng, J. and Chen, C.-L., Spot Cooling Using Electrowetting-Controlled Thin Film Heat Transfer, *3rd International Conference on Micro/Nanoscale Heat and Mass Transfer*, ASME, Paper No. MNHMT2012-75032, pp. 275–281, 2012.

32. Amon, C. H., Yao, S.-C., Wu, C.-F., and Hsieh, C.-C., Microelectromechanical System-Based Evaporative Thermal Management of High Heat Flux Electronics, *J. Heat Transfer*, vol. 127, pp. 66–75, 2005.

33. Kim, J., You, S., and Choi, S. U., Evaporative Spray Cooling of Plain and Microporous Coated Surfaces, *Int. J. Heat Mass Transfer*, vol. 47, no. 14, pp. 3307–3315, 2004.

34. Deng, W. and Gomez, A., Electrospray Cooling for Microelectronics, *Int. J. Heat Mass Transfer*, vol. 54, no. 11, pp. 2270–2275, 2011.

35. Takata, Y., Hidaka, S., Masuda, M., and Ito, T., Pool Boiling on a Superhydrophilic Surface, *Int. J. Energy Res.*, vol. 27, no. 2, pp. 111–119, 2003.

36. Liu, Z. and Qiu, Y., Critical Heat Flux of Steady Boiling for Water Jet Impingement in Flat Stagnation Zone on Superhydrophilic Surface, *J. Heat Transfer*, vol. 128, no. 7, pp. 726–729,

2006.

37. Weibel, J. A., Garimella, S. V., Murthy, J. Y., and Altman, D. H., Design of Integrated Nanostructured Wicks for High-Performance Vapor Chambers, *IEEE Trans. Compon. Packag. Manuf. Technol.*, vol. 1, no. 6, pp. 859–867, 2011.
38. Li, C. and Peterson, G. P., Evaporation/Boiling in Thin Capillary Wicks (II)—Effects of Volumetric Porosity and Mesh Size, *J. Heat Transfer*, vol. 128, pp. 1320–1328, 2006.
39. Li, C., Peterson, G. P., and Wang, Y., Evaporation/Boiling in Thin Capillary Wicks (l)—Wick Thickness Effects, *J. Heat Transfer*, vol. 128, pp. 1312–1319, 2006.
40. Cheng, J.-T. and Chen, C.-L., Adaptive Chip Cooling Using electrowetting on Coplanar Control Electrodes, *Nanoscale Microscale Thermophys. Eng.*, vol. 14, no. 2, pp. 63–74, 2010.
41. Cheng, J.-T. and Chen, C.-L., Active Thermal Management of On-Chip Hot Spots Using EWOD-Driven Droplet Microfluidics, *Exp. Fluids*, vol. 49, no. 6, pp. 1349–1357, 2010.
42. Bar-Cohen, A., Arik, M., and Ohadi, M., Direct Liquid Cooling of High Flux Micro and Nano Electronic Components, *Proc. IEEE*, vol. 94, no. 8, pp. 1549–1570, 2006.
43. Bar-Cohen, A., Gas-Assisted Evaporative Cooling of High Density Electronic Modules, *IEEE Trans. Compon. Packag. Manuf. Technol.*, vol. 18, no. 3, pp. 502–509, 1995.
44. Chinnov, E. A., Kabov, O. A., Zhukovskaya, O. V., and Sharina, I. A., Heat Transfer in a Subcooled Evaporating Liquid Film, *High Temp.*, vol. 44, no. 6, pp. 898–907, 2006.
45. Kabov, O., Lyulin, Yu. V., Marchuk, I. V., and Zaitsev, D. V., Locally Heated Shear-Driven Liquid Films in Microchannels and Minichannels, *Int. J. Heat Fluid Flow*, vol. 28, no. 1, pp. 103–112, 2007.
46. Kabov, O., Gatapova, E. Y., and Zaitsev, D., Cooling technique based on evaporation of thin and ultra thin liquid films, *11th Intersociety Conference on Thermal and Thermomechanical Phenomena in Electronic Systems*, IEEE, pp. 520–527, 2008.
47. Zaitsev, D., Rodionov, D., and O. Kabov, Critical Heat Flux in a Locally Heated Liquid Film Driven by Gas Flow in a Minichannel, *Tech. Phys. Lett.*, vol. 35, no. 7, pp. 680–682, 2009.
48. Chinnov, E. A., Shatskii, E. N., and Kabov, O. A., Evolution of the Temperature Field at the Three-Dimensional Wave Front in a Heated Liquid Film, *High Temp.*, vol. 50, no. 1, pp. 98–105, 2012.
49. Lyulin, Y. V. and Kabov, O., Measurement of the Evaporation Mass Flow Rate in a Horizontal Liquid Layer Partly Opened into Flowing Gas, *Tech. Phys. Lett.*, vol. 39, no. 9, pp. 795–797, 2013.
50. Kabova, Y. O., Kuznetsov, V., and Kabov, O., The Effect of Gravity and Shear Stress on a Liquid Film Driven in a Horizontal Minichannel at Local Heating, *Micrograv. Sci. Technol.*, vol. 21, no. 1, pp. 145–152, 2009.
51. Bartashevich, M., Kabov, O., and Kuznetsov, V., Dynamics of a Finite-Width Liquid Film in a Co-Current Microchannel Gas Flow, *Fluid Dyn.*, vol. 45, no. 6, pp. 924–929, 2010.
52. Kabova, Y. O., Kuznetsov, V., and Kabov, O., Shear-Driven Flow of Locally Heated Viscous Liquid Film in a Minichannel, *Micrograv. Sci. Technol.*, vol. 23, no. 1, pp. 105–112, 2011.
53. Kabov, O., Kabova, Y. O., and Kuznetsov, V., Evaporation of a Nonisothermal Liquid Film in a Microchannel with Co-Current Gas Flow, *Doklady Physics*, vol. 57, no. 10, pp. 405–410, 2012.
54. Kabova, Y. O., Kuznetsov, V., and Kabov, O., Temperature Dependent Viscosity and Surface

Tension Effects on Deformations of Non-Isothermal Falling Liquid Film, *Int. J. Heat Mass Transfer*, vol. 55, no. 4, pp. 1271–1278, 2012.

55. Liu, R. and Kabov, O., Instabilities in a Horizontal Liquid Layer in Cocurrent Gas Flow with an Evaporating Interface, *Phys. Rev. E*, vol. 85, no. 6, 066305, 2012.
56. Plawsky, J. L., Fedorov, A. G., Garimella, S. V., Ma, H. B., Maroo, S. C., Chen, L., and Nam, Y., Nano- and Microstructures for Thin-Film Evaporation—A Review, *Nanoscale Microscale Thermophys. Eng.*, vol. 18, no. 3, pp. 251–269, 2014.
57. Fedorov, A. G. and Meacham, J. M., Evaporation-Enhanced, Dynamically Adaptive Air (Gas)-Cooled Heat Sink for Thermal Management of High Heat Dissipation Devices, *IEEE Trans. Compon. Packag. Technol.*, vol. 32, no. 4, pp. 746–753, 2009.
58. Varanasi, K. K. and Deng, T., Controlling Nucleation and Growth of Water Using Hybrid Hydrophobic-Hydrophilic Surfaces, 12th IEEE Intersociety Conference on Thermal and Thermomechanical Phenomena in Electronic Systems (ITherm), IEEE, pp. 1–5, 2010.
59. Simons, R. E., Estimating the Effect of Flow Bypass on Parallel Plate-Fin Heat Sink Performance, *Electron.-Cooling*, vol. 10, no. 1, 2004.
60. Meacham, J., Ejimofor, C., Kumar, S., Degertekin, F. L., and Fedorov, A. G., Micromachined Ultrasonic Droplet Generator Based on a Liquid Horn Structure, *Rev. Sci. Instrum.*, vol. 75, no. 5, pp. 1347–1352, 2004.
61. Meacham, J., Varady, M. J., Degertekin, F. L., and Fedorov, A. G., Droplet Formation and Ejection from a Micromachined Ultrasonic Droplet Generator: Visualization and Scaling, *Phys. Fluids*, vol. 17, no. 10, 100605, 2005.
62. Forbes, T. P., Degertekin, F. L., and Fedorov, A. G., Multiplexed Operation of a Micromachined Ultrasonic Droplet Ejector Array, *Rev. Sci. Instrum.*, vol. 78, no. 10, 104101, 2007.
63. Narayanan, S., Fedorov, A. G., and Joshi, Y. K., Gas-Assisted Thin-Film Evaporation from Confined Spaces for Dissipation of High Heat Fluxes, *Nanoscale Microscale Thermophys. Eng.*, vol. 13, no. 1, pp. 30–53, 2009.
64. Narayanan, S., Fedorov, A. G., and Joshi, Y. K., On-Chip Thermal Management of Hotspots Using a Perspiration Nanopatch, *J. Micromech. Microeng.*, vol. 20, no. 7, pp. 1–10, 2010.
65. Narayanan, S., Fedorov, A. G., and Joshi, Y. K., Experimental Characterization of a Micro-Scale Thin Film Evaporative Cooling Device, *12th IEEE Intersociety Conference on Thermal and Thermomechanical Phenomena in Electronic Systems (ITherm)*, IEEE, Paper No. IHTC14-23015, pp. 671–674, 2010.
66. Narayanan, S., Fedorov, A. G., and Joshi, Y. K., Interfacial Transport of Evaporating Water Confined in Nanopores, *Langmuir*, vol. 27, no. 17, pp. 10666–10676, 2011.
67. Narayanan, S., Fedorov, A. G., and Joshi, Y. K., Heat and Mass Transfer during Evaporation of Thin Liquid Films Confined by Nanoporous Membranes Subjected to Air Jet Impingement, *Int. J. Heat Mass Transfer*, vol. 58, no. 1-2, pp. 300–311, 2013.
68. de Gennes, P. G., Wetting: Statics and Dynamics, *Rev. Mod. Phys.*, vol. 57, no. 3, pp. 827–863, 1985.
69. Israelachvili, J. N., *Intermolecular and Surface Forces*, Academic, New York, 1992.
70. Rabinovich, Y. I., Derjaguin, B. V., and Churaev, N. V., Direct Measurements of Long-Range Surface Forces in Gas and Liquid Media, *Adv. Colloid Interface Sci.*, vol. 16, no. 1, pp. 63–78, 1982.

71. Derjaguin, B. V., Theory of the Stability of Strongly Charged Lyophobic Sols and the adhesion of Strongly Charged Particles in Solutions of Electrolytes, *Acta Physicochim. USSR*, vol. 14, pp. 633–662, 1941.
72. Verwey, E. J. W., Theory of the Stability of Lyophobic Colloids, *J. Phys. Chem.*, vol. 51, no. 3, pp. 631–636, 1947.
73. Pashley, R. M. and Kitchener, J. A., Surface Forces in Adsorbed Multilayers of Water on Quartz, *J. Colloid Interface Sci.*, vol. 71, no. 3, pp. 491–500, 1979.
74. Deryagin, B. V. and Churaev, N. V., Structure of Water in Thin Layers, *Langmuir*, vol. 3, no. 5, pp. 607–612, 1987.
75. Deryagin, B. V., Popovskii, Y. M., and Goryuk, A. A., Structural Component of Disjoining Pressure in Wetting Films of Nitrobenzene Formed on the Lyophilic Surface of Quartz, *Langmuir*, vol. 3, no. 5, pp. 628–631, 1987.
76. Gee, M. L., Healy, T. W., and White, L. R., Hydrophobicity effects in the condensation of Water Films on Quartz, *J. Colloid Interface Sci.*, vol. 140, no. 2, pp. 450–465, 1990.
77. Pashley, R. M., Hydration Forces between Mica Surfaces in Electrolyte Solutions, *Adv. Colloid Interface Sci.*, vol. 16, no. 1, pp. 57–62, 1982.
78. Ninham, B. W., On Progress in Forces Since the DLVO Theory, *Advances in Colloid and Interface Science*, vol. 83, no. 1-3, pp. 1–17, 1999.
79. Wayner, P. C., Kao, Y. K., and LaCroix, L. V., The Interline Heat Transfer Coefficient of an Evaporating Wetting Film, *Int. J. Heat Mass Transfer*, vol. 19, no. 2, pp. 487–492, 1976.
80. Wayner, Jr, P. C., Effect of Thin Film Heat Transfer on Meniscus Profile and Capillary Pressure, *AIAA J.*, vol. 17, pp. 772–776, 1979.
81. DasGupta, S., Schonberg, J. A., and Wayner, Jr, P. C., Investigation of an Evaporating Extended Meniscus Based on the Augmented Young-Laplace Equation, *ASME J. Heat Transfer*, vol. 115, pp. 201–208, 1993.
82. Buffone, C. and Sefiane, K., Investigation Thermocapillary Convection in Pores and Its Role in Heat and Mass Transfer Enhancement, *Int. J. Multiphase Flow*, vol. 30, pp. 1071–1091, 2004.
83. Buffone, C., Sefiane, K., and Christy, J. R. E., Experimental Investigation of the Hydrodynamics and Stability of an Evaporating Wetting Film Placed in a Temperature Gradient, *Appl. Thermal Eng.*, vol. 24, no. 8-9, pp. 1157–1170, 2004.
84. Buffone, C., Sefiane, K., and Christy, J. R. E., Experimental Investigation of Self-Induced Thermocapillary Convection for an Evaporating Meniscus in Capillary Tubes Using Micro–Particle Image Velocimetry, *Phys. Fluids*, vol. 17, 052104, 2005.
85. Dhavaleswarapu, H. K., Chamarthy, P., Garimella, S. V., and Murthy, J. Y., Experimental Investigation of Steady Buoyant-Thermocapillary Convection near an Evaporating Meniscus, *Phys. Fluids*, vol. 19, 082103, 2007.
86. Chamarthy, P., Dhavaleswarapu, H. K., Garimella, S. V., Murthy, J. Y., and Wereley, S. T., Visualization of Convection Patterns near an Evaporating Meniscus Using μPIV, *Exp. Fluids*, vol. 44, no. 3, pp. 431–438, 2008.
87. Dhavaleswarapu, H. K., Garimella, S. V., and Murthy, J. Y., Microscale temperature Measurements near the Triple Line of an Evaporating Thin Liquid Film, *J. Heat Transfer*, vol. 131, no. 6, 061501, 2009.

88. Wang, H., Murthy, J. Y., and Garimella, S. V., Transport from a Volatile Meniscus Inside an Open Microtube, *Int. J. Heat Mass Transfer*, vol. 51, no. 11-12, pp. 3007–3017, 2008.
89. Wee, S. K., Kihm, K. D., and Hallinan, K. P., Effects of the Liquid Polarity and the Wall Slip on the Heat and Mass Transport Characteristics of the Micro-Scale Evaporating Transition Film, *Int. J. Heat Mass Transfer*, vol. 48, no. 2, pp. 265–278, 2005.
90. Dhavaleswarapu, H. K., Murthy, J. Y., and Garimella, S. V., Numerical Investigation of an Evaporating Meniscus in a Channel, *Int. J. Heat Mass Transfer*, vol. 55, no. 4, pp. 915–924, 2012.
91. Do, K. H., Kim, S. J., and Garimella, S. V., A Mathematical Model for Analyzing the Thermal Characteristics of a Flat Micro Heat Pipe with a Grooved Wick, *Int. J. Heat Mass Transfer*, vol. 51, no. 19, pp. 4637–4650, 2008.
92. Wang, H., Garimella, S. V., and Murthy, J. Y., Characteristics of an Evaporating Thin Film in a Microchannel, *Int. J. Heat Mass Transfer*, vol. 50, no. 19, pp. 3933–3942, 2007.
93. Wang, H., Garimella, S. V., and Murthy, J. Y., An Analytical Solution for the Total Heat Transfer in the Thin-Film Region of an Evaporating Meniscus, *Int. J. Heat Mass Transfer*, vol. 51, no. 25, pp. 6317–6322, 2008.
94. Schrage, R. W., *A Theoretical Study of Interphase Mass Transfer*, Columbia University Press, New York, 1953.
95. Skinner, L. M. and Sambles, J. R., The Kelvin Equation—A Review, *J. Aerosol Sci.*, vol. 3, no. 3, pp. 199–210, 1972.
96. Fisher, L. R., Forces Due to Capillary-Condensed Liquids: Limits of Calculations from Thermodynamics, *Adv. Colloid Interface Sci.*, vol. 16, no. 1, pp. 117–125, 1982.
97. Fisher, L. R., Gamble, R. A., and Middlehurst, J., The Kelvin Equation and the Capillary Condensation of Water, *Nature*, vol. 290, no. 5807, pp. 575–576, 1981.
98. Fisher, L. R. and Israelachvili, J. N., Experimental Studies on the Applicability of the Kelvin Equation to Highly Curved Concave Menisci, *J. Colloid Interface Sci.*, vol. 80, no. 2, pp. 528–541, 1981.
99. Swanson, L. W. and Herdt, G. C., Model of the Evaporating Meniscus in a Capillary Tube, *ASME J. Heat Transfer*, vol. 114, no. 2, pp. 434–441, 1992.
100. Wayner, Jr, P. C., Kao, Y. K., and LaCroix, L. V., The Interline Heat-Transfer Coefficient of an Evaporating Wetting Film, *Int. J. Heat Mass Transfer*, vol. 19, no. 5, pp. 487–492, 1976.
101. Philip, J. R., Unitary Approach to Capillary Condensation and Adsorption, *J. Chem. Phys.*, vol. 66, pp. 5069–5075, 1977.
102. Derjaguin, B. V. and Churaev, N. V., Structural Component of Disjoining Pressure, *J. Colloid Interface Sci.*, vol. 49, no. 2, pp. 249–255, 1974.
103. Langmuir, I., Repulsive Forces between Charged Surfaces in Water and the Cause of the Jones-Ray Effect, *Science*, vol. 88, no. 2288, pp. 430–432, 1938.
104. Kumar, D. and Biswas, S. K., Contribution of Different Physical Forces to the Disjoining Pressure of a Thin Water Film Being Pressed by an Oil Droplet, *J. Colloid Interface Sci.*, vol. 348, no. 1, pp. 255–264, 2010.
105. Lu, Z., Narayanan, S., and Wang, E. N., Modeling of Evaporation from Nanopores with Nonequilibrium and Nonlocal Effects, *Langmuir*, vol. 31, no. 36, pp. 9817–9824, 2015.